Grant number: FA9550-17-1-0019

Research Title: **Auroral Thermosphere Density Study**

PI: Anasuya L. Aruliah

Period of performance: 15th December 2016-14th April 2018

Table of Contents

List of Figures

Figure 10 The 42m magnetic field-aligned dish of the EISCAT Svalbard Radar measurements of the height distribution of ionospheric parameters are shown here for the period 00-06 UT on 27 January 2017. a) electron densities; b) ion temperatures c) the line-of-sight component of the plasma speed along the magnetic field $V_{//}$; and d) the Tromsø VHF radar line-of-sight plasma velocities pointing northward, with elevation 30°.

Figure 11 A direct comparison of the 42m ESR measurement of the plasma speed $V_{//}$ with the FPI measured vertical wind U_z for Longyearbyen 01-04 UT on 27 January 2017.

Figure 12 a) The height distribution of neutral densities for 00-06 UT on 27 January 2017, derived from the ESR 42m dish measurements of electron densities, using the simplified momentum equation. b) Comparison of ESR-derived neutral densities with NRLMSISE-00 for atomic oxygen [O] for the period 00-06 UT on 27 January 2017.

Figure 13 FPI observations from Longyearbyen for the periods 14:00-15:00 UT and 02:00-04:00 UT on the night of 29-30 January 2017 are presented here. Cloudy periods have been removed. This was a geomagnetically quiet period with Kp = 2^- and 1^o, respectively, as is indicated by the smaller perturbations of the x-component of the Earth's magnetic field shown in c) IMAGE magnetometer chain measurements for the night of 29-30 January 2017.

Figure 14 The 42m magnetic field-aligned dish of the EISCAT Svalbard Radar measurements of the height distribution of ionospheric parameters are shown here for the period 14-15 UT on 29 January 2017. a) electron densities; b) ion temperatures and d) the line-of-sight component of the plasma speed $V_{//}$.

Figure 15 The 42m magnetic field-aligned dish of the EISCAT Svalbard Radar measurements of the height distribution of ionospheric parameters are shown here for the period 02-04 UT on 30 January 2017. a) electron densities; b) ion temperatures and d) the line-of-sight component of the plasma speed $V_{//}$.

Figure 16 A direct comparison of the 42m ESR measurement of the plasma speed $V_{//}$ interpolated to the FPI measured vertical wind U_z for Longyearbyen at a) 13-16 UT and b) 01-04 UT on 27 January 2017.

Figure 17 CMAT2 latitude versus time plots of the development of the top pressure level on 27 January 2017 at the Svalbard longitude (~18°E) after a localised heating event. a) Shows the height of the pressure level; b) vertical wind relative to the pressure level; c) rate of change of height of the pressure level; d) absolute vertical wind.

Figure 18 CMAT2 simulations at a fixed altitude of 300 km (similar to a satellite at fixed altitude) taking the ratio of the simulation of the heating event against a control without heating. a) Shows that the neutral temperature is raised by up to 20% in the polar regions during the upwelling. b) Shows the equivalent for the neutral density, which is over 20% larger during the heating event.

Figure 19 Preliminary results of O+ number densities measured by the INMS on the PHOENIX CubeSat compared with the CMAT2 model of atomic oxygen at constant height 300 km.

List of Tables

Summary

Atmospheric drag is the 2nd largest perturbation on satellite orbits, after the gravitational force of an oblate Earth. Atmospheric drag occurs where the satellite enters the top layer of the Earth's atmosphere, the thermosphere, which means an altitude below around 300 km at solar minimum, and around 800 km at solar maximum. The concern of our project is the "lumpiness" of thermospheric density. In particular, mesoscale density structures in the polar regions are poorly represented by empirical atmospheric models used in satellite orbit determination. They do not allow for heating from electrical currents generated by the solar wind-magnetospheric dynamo in the auroral regions. Heating causes upwelling of the denser air which can be observed by Fabry-Perot Interferometers measuring the vertical winds. On either side of a heating region there is downwelling as the atmosphere relaxes back to a normal state. Physics-based models are better able to represent the meso-scale structures, but are far too slow to be useful for orbit prediction. Two nights are presented here as case studies to indicate the size of vertical winds and the horizontal extent of up and downwelling regions for geomagnetically quiet and active conditions. We also use the UCL Coupled Middle Atmosphere Thermosphere (CMAT2) model to estimate the changes in density from a localised heat source, representative of auroral plasma flows. Finally we present initial results from the PHOENIX CubeSat which was one of the QB50 constellation of CubeSats launched in the summer of 2017. PHOENIX carries a miniaturised mass spectrometer, with the aim to provide the first in-situ mass spectrometer measurements since the Dynamics Explorer in the early 1980s.

The proposed objectives were:

1) Set up the FPIs to be calibrated and ready for the experiment, and in a fit state to continue monitoring the upper thermosphere and extending the dataset of auroral measurements to provide context for the experiment.
2) Carry out a 24 hour experiment using the network of Fabry-Perot Interferometers (FPIs) with the EISCAT and SuperDARN radars to provide a case study to investigate the density variation of the upper thermosphere in the auroral and polar cap region.
3) Undertake a modelling study using the UCL CMAT2 global circulation model to investigate the contribution of frictional heating in the auroral zones to the density variation.
4) Prepare a set of CMAT2 model simulations to be used to estimate the size of orbit perturbations and to compare with conventional satellite drag models.

These objectives were all achieved and highlights are listed below.

- Field campaign trip to the KEOPS and Sodankylä FPI sites 9-27 January 2018
- Dr Ian McWhirter consultancy for instrumental work and maintenance for the field trip
- EISCAT mainland and ESR radar experiments:
    1. 16UT on 28 Jan 2017 – 04UT on 29 Jan 2017 (ESR CP2 and
    2. 16UT on 30 Jan 2017 – 04UT on 31 Jan 2017

- Related activities: 3 invited talks, 3 talks, 1 poster and 2 4th year undergraduate projects (see reference list)
- Extended the grant period by 4 months to 14 April 2018, in order to include the first of 2 QB50 Incoherent Scatter World Day periods (January 2018)

1. Introduction

Atmospheric drag is the 2nd largest perturbation on satellite orbits, after the gravitational force of an oblate Earth. Atmospheric drag occurs where the satellite is below around 300 km altitude at solar minimum and around 800 km at solar maximum. This large range of heights is because the thermosphere, which is the uppermost layer of the Earth's atmosphere, expands and contracts radically with the approximately 11 year cycle of solar activity. Above this height solar photon pressure dominates. On a much shorter time scale in the auroral regions, the solar wind-magnetospheric dynamo can suddenly dump hundreds of GigaWatts of power during a geomagnetic storms and substorms that could last for hours to days. This drives electrical currents that flow through the ionosphere and heat the thermosphere through frictional heating (also commonly called Joule heating). This is the same physics as for an electric heater where the electric current through a highly resistive wire creates heat. As a result, thermospheric temperatures in the auroral regions can quickly (< 1 hour) double to reach up to 2000 K, with the atmosphere expanding upwards in tandem by a few hundred km (Dobbin et al., 2006). This can perturb the orbits of Low Earth Orbit (LEO) satellites and space debris, potentially leading to collisions and un-controlled re-entry over populated areas.

Satellite orbits are tracked using Two Line Elements (TLEs) that can be found on the website https://www.celestrak.com/NORAD/elements/ run under the auspices of NORAD (North American Aerospace Defense Command) founded by the USA and Canada to provide warning of atmospheric threats over North America. The TLEs are a list of basic information determined on the assumption that the satellite is in an elliptical orbit. The list includes the eccentricity, orbit inclination, mean motion (revolutions per day) and a satellite drag term (e.g. see descriptive article https://www.celestrak.com/columns/v04n03/). These are used to predict the orbit. The TLEs need to be updated regularly when new information becomes available from GPS or radar tracking. As a result of atmospheric drag, LEO satellites drop lower. Through conservation of momentum they then move faster. In order to maintain orbits, LEO satellites have to boost their orbits around 4 times a year, and during periods of high solar activity the orbit adjustments may be every few weeks. The success of the TLE prediction relies on how realistic is the atmosphere model

The concern of our project is the "lumpiness" of the thermospheric density. The atmospheric gas expands upwards above a heating source. The expansion is not uniformly outwards in all directions, because the atmosphere below is exponentially more dense than that above. Consequently the gas rises until it reaches an upper limit where gravity balances the expansion, and then it falls to the side of the heat source. This creates a vertical convection cell which we can measure as vertical winds using Fabry-Perot Interferometers. The consequence of upwelling gas is that it brings denser air upwards, thus creating a local region of higher density gas. The satellite orbits at a roughly constant altitude and so ploughs through this denser region and suffers increased atmospheric drag and orbit perturbation. This is vividly illustrated by Figure 1, which is a contour map of the altitude of the top layer of the atmosphere in the auroral region covering the location of our observing sites at Longyearbyen and Kiruna (latitudes 60-90° N and longitude 0-20° E). The contour colour is the neutral temperature, which is proportional to the density from the Ideal Gas Law. Arrows indicate the direction of the neutral winds, which are dominated by meridional winds flowing equatorwards. In order to show the vertical winds clearly, this component has been multiplied by a factor of 10.

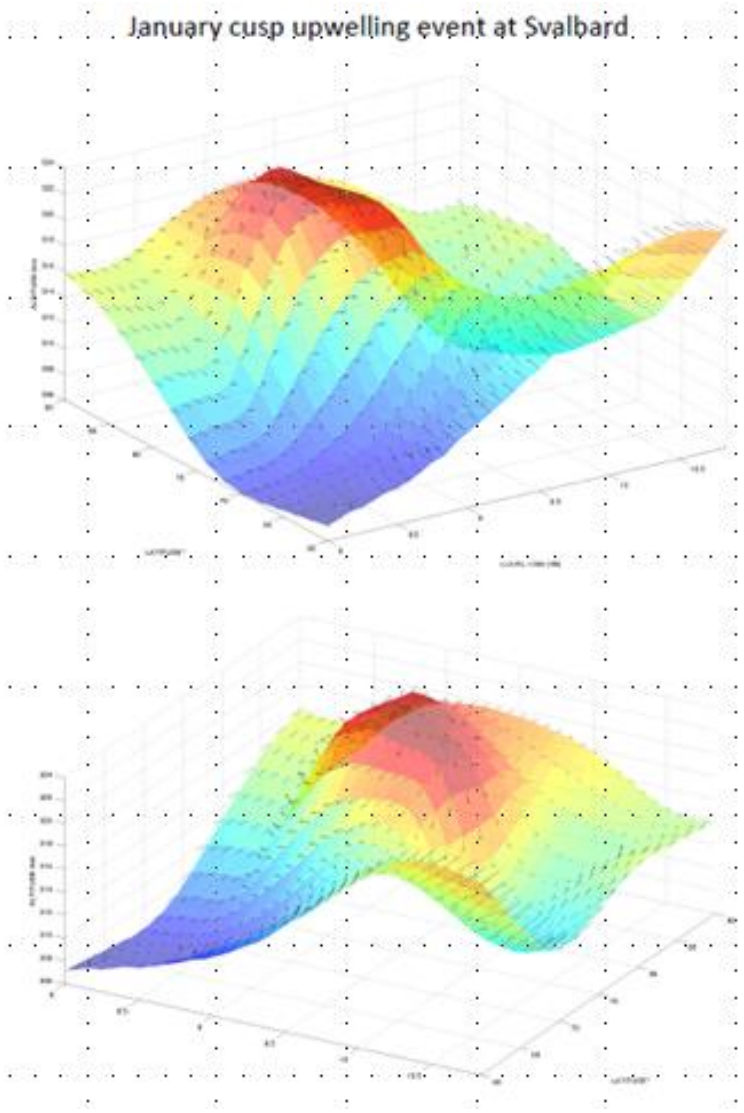

Figure 1 CMAT2 model simulation of a cusp upwelling simulation, showing the altitude of the top surface of the thermosphere; the neutral temperature, and neutral winds (where the vertical component is multiplied by a factor 10 for clarity). a) Shows increase in vertical winds as expansion of atmosphere takes place over this region. (NB meridional wind dominates, and vertical wind multiplied by 10 for clarity.). b) shows after heating effect is turned off, we see strong(er) downwards winds as the atmosphere returns to normal. (NB meridional wind dominates, and vertical wind multiplied by 10 for clarity.)

There are several sources of heating which cause the atmosphere above the heat source to expand. The three greatest heating sources for the auroral thermosphere, in order of magnitude, are solar heating, Joule heating and auroral particle precipitation. With the three previous EOARD-funded projects we focussed on Joule heating caused by auroral activity at high latitudes, i.e. in the magnetic cusp region near the North Pole at Longyearbyen, Svalbard and the auroral region in Kiruna, Sweden. In this project we will look into the extent of the high latitude heating region, and also touch on a major heating source, which are the tides from solar heating that propagate upwards from the troposphere and stratosphere. The critical difference between auroral and tidal heating are that tides are fairly predictable, since they are harmonics of the 24 hour day-night heating cycle – with 24h, 12h and 8h being the dominant tidal modes (e.g. England, 2011). In contrast the Joule heating depends on the geomagnetic activity of the Sun, which is not easily predicted. The Joule heating depends on the conductivity of the atmosphere and applied electric fields. The underlying conductivity of the auroral ionosphere is enhanced by the entry of energetic particles from the solar wind, and the electric fields are generated by the solar wind-magnetospheric dynamo.

The polar regions are poorly represented by atmospheric models used in satellite orbit determination such as the Jacchia-Bowman satellite drag model (e.g. Bowman et al., 2008) and the Drag Temperature Model (e.g. Bruinsma et al, 2011). These are empirical models, and are limited by a

scarcity of observations in the polar regions owing to inclement and inaccessible ground conditions. Much of the measurements necessarily come from the combination of multiple overhead passes of polar orbiting satellites. Consequently the empirical models of the polar regions are over-smooth and lack structure. Physics-based models are better able to represent the meso-scale structures, on spatial scales of the order of 100's km, and temporal variations on the order of minutes; but these are far too slow to be useful for orbit prediction. The empirical models are able to determine densities in seconds compared with a few hours for a calculation from a physics-based model.

A case study experiment and modelling study were proposed for a 1 year study on a modest budget, in preparation for a collaboration between the APL team and experts in satellite orbit determination. A no-cost extension was granted to allow us to include data from a recent launch of 36 CubeSats – the QB50 mission. These CubeSats carry the first mass spectrometers since the DE-1 and DE-2 satellites of the 1980s, and will allow us to calibrate the models. This is of particular importance because we are in a period of extended very low solar activity, while the period between the launch of the first satellites in 1957 to the early 2000s were a period of a Grand Solar Maximum. The empirical models such as NRLMSISE-00 (Picone et al., 2002) and HWM (Drob et al., 2008) are largely based on measurements made during the Grand Solar Maximum period.

The accuracy of tracking satellite orbits and the location of space debris depends on many parameters, including the choice of atmospheric models. Vallado and Finkleman (2014) wrote an overview assessing satellite drag modelling. Satellite drag models are designed for rapid performance by being based on the average behaviour (climatologies) of the upper atmosphere as observed by a limited set of ground-based instruments and satellites. Physics-based models are not used for real-time orbit tracking since they can take hours to calculate density, but they are critical for understanding the underlying mechanism of atmospheric behaviour. This project will focus on persistent structures in the density of the upper atmosphere that are on the scale size of a few hundred kilometres that can last for hours. In particular, we will study structures in the region close to the magnetic poles of the Earth, where the dynamic solar wind controls the quantity, energy and motion of particles in the upper atmosphere. Satellite drag models poorly model the polar regions, and do not adequately identify density bulges caused by localised sources of high latitude/auroral heating. Persistent density structures are likely to cause systematic perturbations in the orbits of not only satellites, but also space debris; but the size of such perturbations are unknown without suitable model simulations.

2. Methods, Assumptions and Procedures

In this report we present 2 case studies of observations made on the nights of 26-27 January 2017 and 29-30 January 2017. The former is during geomagnetically disturbed conditions (Kp 4^{+}) and the latter is geomagnetically quiet (Kp 1^{o}) though post-substorm. We have already successfully carried out 3 coordinated FPI-EISCAT radar experiments to investigate density perturbations in the magnetic cusp region (Aruliah, 2012, 2013) and the auroral magnetic midnight region (Aruliah, 2016), which were funded by small US Air Force grants under the scheme overseen by the EOARD. These studies were initiated by CHAMP satellite observations of an anomalous density bulge in the thermosphere over the magnetic cusp (Lühr et al., 2004). We carried out the first two FPI-EISCAT experiments at Longyearbyen to test the theory of Carlson et al. (2012a) that considerable upwelling is possible if thermospheric heating occurs in the altitude region 150-200 km. Figure 2 is taken from Carlson et al. (2012) and shows the energies associated with particles that penetrate the atmosphere to different depths. Our interest is in the different heating influences between soft and hard precipitation, i.e. particle precipitation where energy is dumped in the altitude region 150-200 km

(soft precipitation) and between 100-120 km (hard precipitation). The conditions of soft precipitation are met by the magnetic cusp region, as illustrated by Figure 3, which is taken from a paper presenting a new empirical model of Poynting flux by Cosgrove et al (2014). The red hot spot shows the cusp energy influx of the order of 4 mW m^{-2} under Interplanetary Magnetic Field conditions of Bz north and low geomagnetic activity. The cusp is the dominant feature under such quiet conditions. The mapping of Poynting flux is fixed in the Sun-Earth geometry by magnetic field lines. The yellow and red dashed lines show the paths of the FPI sites at Longyearbyen and Kiruna, respectively, as the Earth rotates under this pattern. Longyearbyen passes near or under the cusp, and is the only location where there are both incoherent scatter radars (ISR), and also the UCL FPIs.

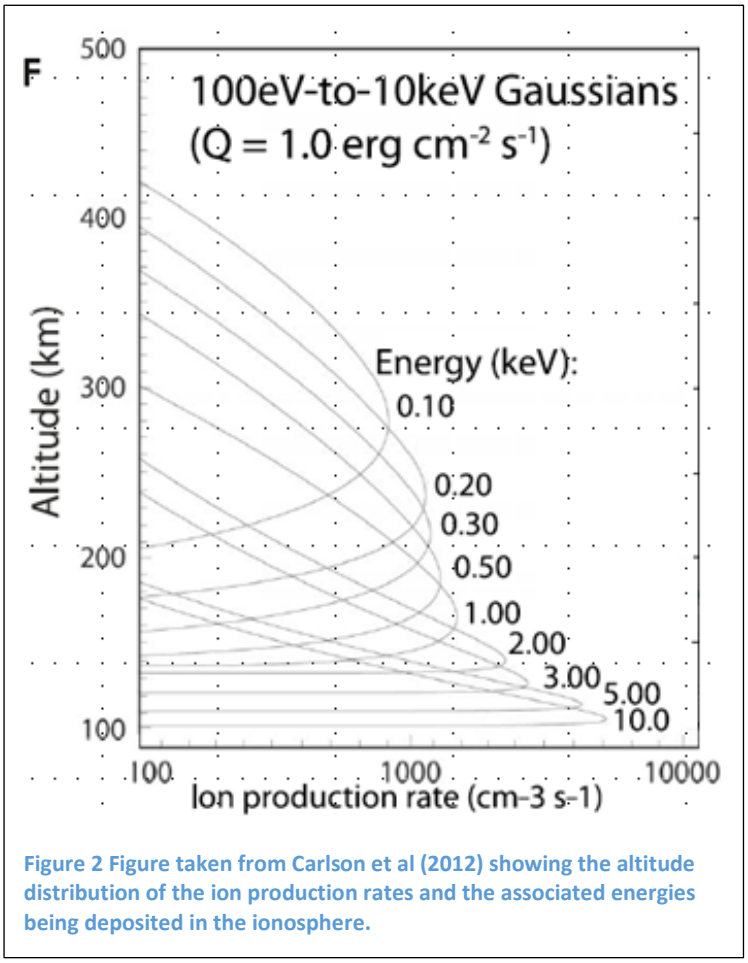

Figure 2 Figure taken from Carlson et al (2012) showing the altitude distribution of the ion production rates and the associated energies being deposited in the ionosphere.

The first two FPI-EISCAT experiments have shown that unexpectedly large vertical winds were observed by the FPI, at the same time as soft precipitation and fast plasma flows were observed by EISCAT. The third FPI-EISCAT experiment was undertaken using the UCL FPIs at Kiruna and Sodankylä, which are auroral oval sites. A second radar, the Kilpisjärvi Atmospheric Imaging Receiver Array (KAIRA), provided additional line-of-sight VHF radar measurements along the beam of the EISCAT Tromsø radar in order to determine plasma velocities bi-statically in the altitude range 150-200km (McKay-Bukowski et al., 2015). The aim was to test whether upwelling was possible with hard precipitation too. A parallel CMAT2 model study was undertaken, which indicated that upwelling was possible, but much less. The observations from the FPI-EISCAT-KAIRA did not show upwelling unambiguously. The presence of cloud meant we decided to exclude a period from 21:20-22:40 UT when there appeared to be upwelling up to 60 ms^{-1} at the same time as soft particle precipitation and fast plasma flows. The need to identify the presence of cloud is the reason for the installation of cloud sensors, as described below. In addition to the final reports to EOARD, some results have been reported in Ronksley (UCL PhD, 2016) and also in conferences (e.g. Carlson et al., 2012b, Aruliah et al, 2014, 2015).

Our longer-term aim is that the CMAT2 model simulations that result from the study will feed into a satellite drag collaboration with experts in satellite drag research. We have already made contact with Prof Marek Ziebart in the UCL Department of Civil, Environmental and Geomatic Engineering and Dr Stuart Grey at the University of Strathclyde, Scotland. We have jointly supervised undergraduate projects: Dr Aruliah was 1st supervisor, with Dr Grey as 2nd supervisor, for a UCL

International Students Dean's Summer Student Scholarship awarded to a student from the Indian Institute of Technology (Bombay) in 2015; and for an Astrophysics 4th year project in the academic year 2015-2016. Dr Aruliah also recently was one of the two PhD examiners for Prof Ziebart's student, in order to bring an atmospheric modelling perspective.

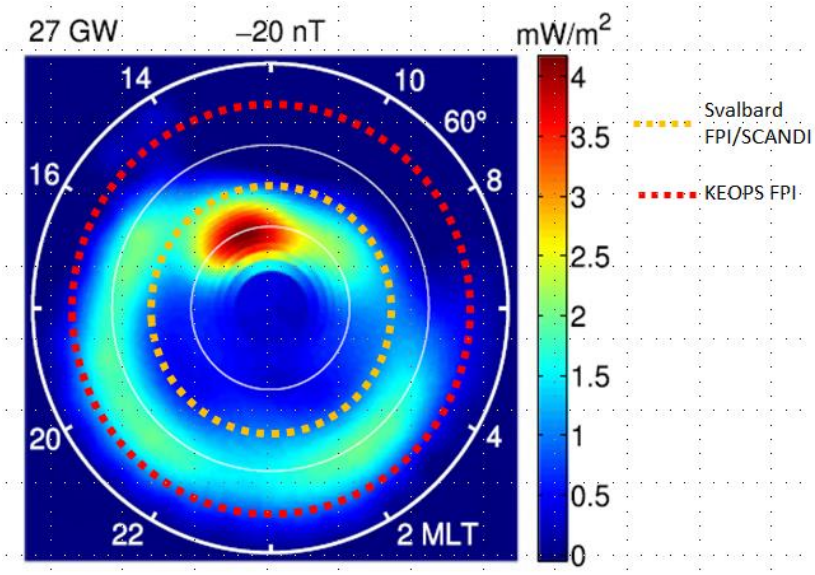

Figure 3 Figure adapted from Cosgrove et al. (2014) of their new Poynting flux empirical model for low geomagnetic activity using FAST satellite measurements. The paths of the sites at Longyearbyen (yellow) and Kiruna (red) are shown as the Earth rotates under the the fixed Sun-aligned configureation set up by the solar wind-magnetospheric dynamo.

We also have contributed to the science of the QB50 mission (www.qb50.eu) funded by a European Union FP7 grant of € 9M as a technology demonstrator. Dr Aruliah was on the Science Working Group. We requested a 4 month extension to allow us to look at the first Ion-Neutral Mass Spectrometer data output from one of the 36 CubeSats that were launched in summer 2017.

2.1 Fabry-Perot Interferometers at Kiruna and Sodankylä: the maintenance visit, 9-27 January 2017

We have used observations from the University College London (UCL) network of Fabry-Perot Interferometers (FPIs) and EISCAT radars in Arctic Scandinavia. Figure 3 shows the locations of the FPIs at Longyearbyen, Kiruna and Sodankylä and also photographs of the observatories and a cloud sensor. Figure 3 is taken from Cosgrove et al. (2014) showing an empirical model of Poynting flux from the solar wind-magnetospheric dynamo, focussing on northward solar wind magnetic field, and low geomagnetic activity. Under these conditions the dominant energy feature is in the cusp, and the auroral oval region has less than a quarter of the Poynting flux measured during active state conditions. The orientation of this pattern of the Poynting flux is fixed in the Sun-Earth direction, and in geomagnetic coordinates. The yellow dashed line shows the path of Longyearbyen as the Earth rotates in an anti-clockwise direction, and the red line is Kiruna. Thus our FPIs and the EISCAT radars are well positioned to observe a full range of auroral behaviour, from the polar cap region (open magnetic field lines) to the auroral oval (regions connected to merging and reconnection of solar wind and magnetospheric magnetic field lines).

The FPIs measured thermospheric winds and temperatures, and the radars measured the plasma properties of the auroral ionosphere. There are 4 fixed gap etalon, narrow field FPIs (1° field of view, single look direction) and one wide-field FPI, with a variable etalon gap, called a Scanning Doppler Imager (SCANDI, 150° field of view). These are distributed at 3 observatories. Two narrow field

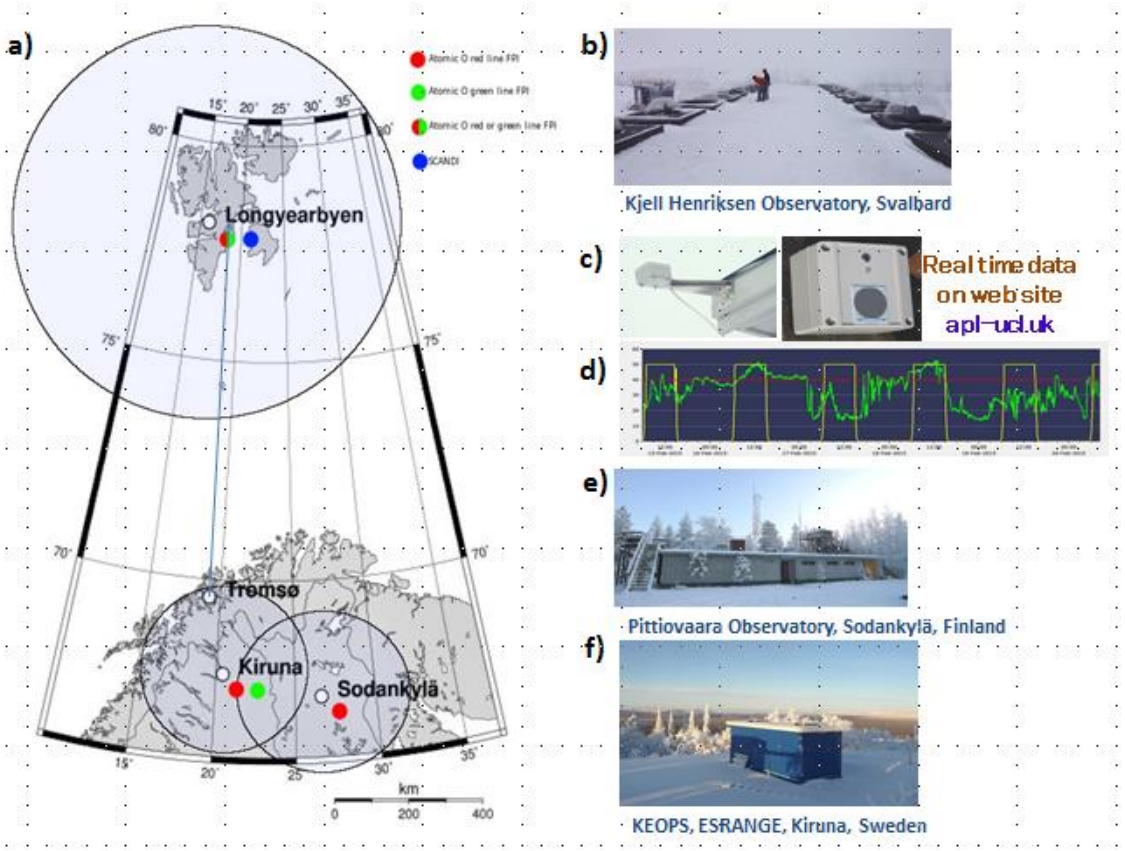

Figure 4 a) Map of the locations of the FPIs at b) Longyearbyen (Kjell Henriksen Observatory), e) Sodankyla (Pittiovaara Observatory) and f) Kiruna (KEOPS, ESRANGE). Also photos of c) the Cloud Sensor and d) output data.

FPIs are on the ESRANGE rocket range near Kiruna, Sweden, (67.88°N, 21.03°E) with one observing the red line airglow emission at 630.0nm and the other observing the green line 557.7nm emission. The narrow field FPI at the Sodankylä Geophysical Observatory in Finland (67.4°N, 26.6°E) observes the red line. The narrow field FPI and SCANDI at the Kjell Henriksen Observatory at Longyearbyen, Svalbard, (78.15°N, 16.04°E) are capable of observing either the red or green line. The circles represent the field of view of the FPI observations when observing the red line. It is assumed that the red line emission has a peak intensity at around 240 km altitude (e.g. Vlasov et al., 2005), and the Kiruna and Sodankylä FPIs have a pointing direction inclined at 45° elevation from the ground, while the Longyearbyen FPI is inclined at 30° elevation. The SCANDI field of view allows it to map winds and temperatures across the whole sky simultaneously. Meanwhile the narrow field FPIs use a rotating mirror to observe in a sequence of look directions, for example, North, East, South, West, Zenith. The observations are made during the hours of darkness (solar zenith angle > 98°) since the auroral and airglow emissions are only a few hundred times brighter than starlight. The photons are recorded by highly sensitive Electron Multiplying Charge Coupled Devices (EMCCD) which allows short exposure times, typically 30 or 60 seconds, but as low as 10 seconds (Ford et al., 2007). The complete sequence of look directions for the narrow field FPI is around 8 minutes. The SCANDI requires 5 complete scans of the etalon gap to collect sufficient photons for each of the sectors that are mapped onto the sky. So a complete sky image takes 7-8 minutes to compile, consequently smoothing out thermospheric variability, but giving information on spatial variability to around 100 km resolution.

The UCL instruments have been maintained for many years by Dr Ian McWhirter, a former employee of UCL and originally responsible for designing and building them. It is now a policy of the UCL Physics Department that professional technical expertise should not generally be retained in-house, hence the need to employ Dr McWhirter on a contract / consultancy basis as and when required. Dr McWhirter also presents the results from these instruments at conferences, especially the Annual European Meeting for Atmospheric Studies in Optical Methods. He presented a paper enabled by the work carried out on this trip at the meeting in Barcelona, Spain in September 2017 (McWhirter and Aruliah, 2017).

At the start of 2017, the instruments at the KEOPS site at the ESRANGE rocket range near Kiruna, Sweden and the Geophysical observatory in Sodankylä, Finland were long overdue for maintenance. The last visit to KEOPS had been two years previously and Sodankylä six years. The three week visit was based at ESRANGE, with one week spent at Sodankylä, which is a six hour drive away (hire car is the only practical way to travel between the two locations). The instruments run continuously during hours of darkness and are operated and monitored remotely over the Internet. They have proved to be extremely reliable. However, some repairs were inevitably required.

The instruments are: KEOPS: Red line and green line Fabry Perot interferometers, all-sky colour camera and infra-red cloud sensor. Sodankylä: Red line Fabry Perot Interferometer and all-sky colour camera, plus cloud sensor installed this visit.

The aims of the visit were as follows:

i) **Routine maintenance of instruments:** All the optics and domes were inspected and thoroughly cleaned. All mechanical parts were checked for smooth running. The parallelism of the three Fabry-Perot etalons was tested and adjusted as necessary. Temperature controllers were checked for correct operation. Many other minor housekeeping tasks were carried out.

ii) **Computing:** All computers needed to be updated and checked, including replacing the old WinXP operating system on some machines. Software improvements were implemented. An interface problem with the KEOPS All-Sky camera was diagnosed and corrected. The computer for the Sodankylä FPI had failed completely and was replaced.

iii) **Repairs:** Known problems had to be diagnosed beforehand as far as possible so the correct spares could be brought. Repairs were carried out as follows:
   a) KEOPS Red line FPI: The scanning mirror would not turn round. This turned out to be due to the (very old) motor which had seized. A new motor of an improved specification was fitted. The etalon pressure scanning system was leaking so the o-ring seals in the vacuum components were replaced with new ones.
   b) KEOPS Green line FPI: The filter wheel would not turn round. This was due to a seized bearing which was replaced and lubricated. The motor was also replaced as the fault had subjected it to undue stress.
   c) Sodankylä FPI: A problem with the calibration lamp control was found to be caused by a faulty chip which was replaced.

iv) **Improvements:** An improved calibration lamp was fitted to the KEOPS red FPI. A cloud sensor of the type already installed at KEOPS was installed at Sodankylä. Webcams were installed to facilitate remote monitoring of the instruments.

2.2 Cloud Sensors and the need for clear skies

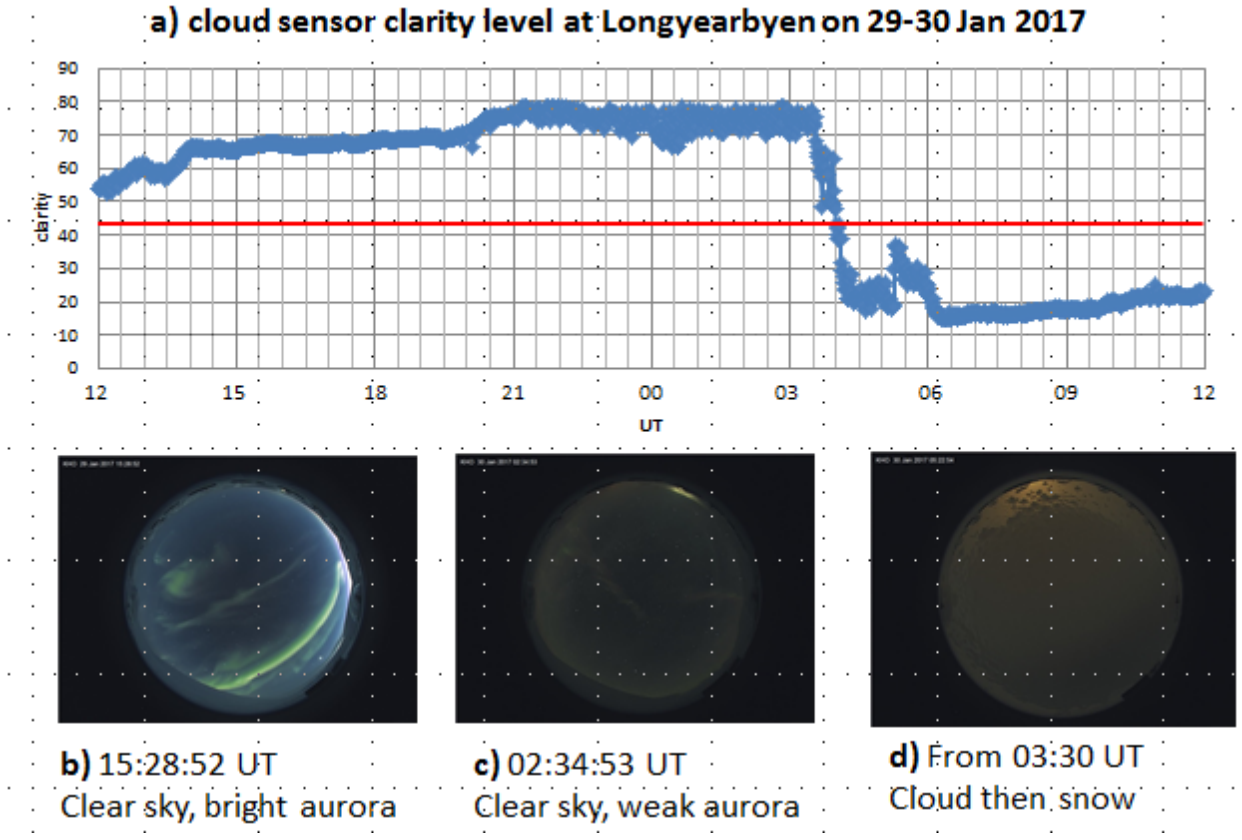

Figure 5 a) The sky clarity measurement from the cloud sensor at Longyearbyen on the night of 29-30 January 2017. Figures b-d show sample images from the UCL all-sky imager at Longyearbyen to illustrate the actual cloud conditions at these times: b) clear sky, bright aurora; c) clear sky, weak aurora and d) cloud and snow.

Figure 5a shows the output from the cloud sensor at Longyearbyen for night of 29-30 January 2017, where there is a distinct difference between clear and cloudy periods. Comparison with the all-sky camera was made to determine a minimum appropriate clarity level to indicate that the skies were indeed clear. Three examples of all-sky images are shown (Figures 5b-d). Before 04UT on 30 Jan 2017, the clarity value was greater than 50%, which, when compared with the all-sky images, seems to be a level indicating clear skies. Afterwards the value dropped sharply to around 20%, indicating cloud. The clarity value is obtained by taking a ratio of the temperature measured by the cloud sensor pointing down to the ground, and up to the sky. A high ratio indicates a cold sky, i.e. clear sky conditions. However, the value of this ratio is not necessarily the same at all sites. Also, if the cloud sensor gets covered in snow, which doesn't melt, then a false cloudy reading is given. Under these circumstances, it is unlikely that a false "clear sky" reading is possible.

Figure 6 shows the clarity levels for all three sites during January 2017. The viewing conditions were generally poor for this month, with few periods showing clarity > 50% for Sodankylä, none for

KEOPS and only around half for Longyearbyen. We require clear skies, and darkness to measure neutral winds with the FPIs, otherwise cloud scatter contaminates the Doppler shift measurements.

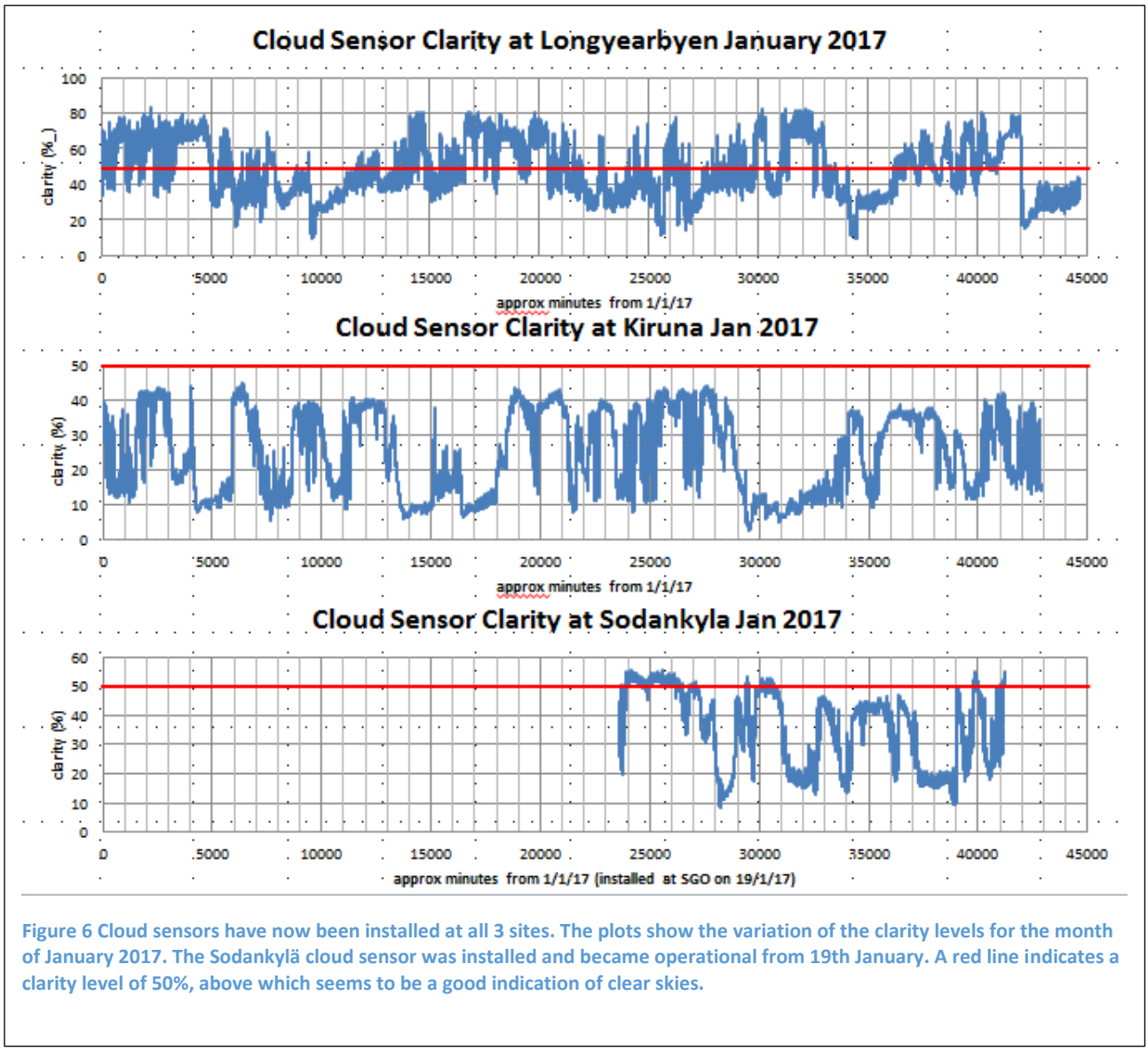

Figure 6 Cloud sensors have now been installed at all 3 sites. The plots show the variation of the clarity levels for the month of January 2017. The Sodankylä cloud sensor was installed and became operational from 19th January. A red line indicates a clarity level of 50%, above which seems to be a good indication of clear skies.

2.3 EISCAT radar experiments

The European Incoherent Scatter (EISCAT) radars are three of ten incoherent scatter radars in the world. The EISCAT radars used for the case studies were the EISCAT Svalbard Radar (500 MHz) at Longyearbyen and the VHF radar (224 MHz) at Tromsø (locations shown in Figure 3). The ESR is co-located with the UCL FPI and SCANDI. The 42m dish measured the ion and electron temperatures, electron densities and line-of-sight plasma velocities along the magnetic field line. The VHF pointed north towards Svalbard, at an elevation of 30°.

The FPI and EISCAT radar measurements provided ion and neutral atmosphere measurements that were combined to determine the energy input and estimate the neutral density of the thermosphere. We used the method of Vickers et al (2013) where the thermospheric neutral density is determined from the simplified momentum equation. A preliminary study was carried out by Dr Aruliah's MSci project student, Jennifer Hall (Hall, 2016), and we have based the analysis on her programmes.

2.3 Coupled Middle Atmosphere Thermosphere (CMAT2) model

The UCL Coupled Middle Atmosphere model (CMAT2) was used to simulate the case study (e.g. Harris et al., 2002). From this short study, the aim was to create a set of model simulations to present to colleagues who are experts in satellite orbit determination to estimate the size of orbit perturbations from persistent structures. The CMAT2 simulations can then be used to compare with conventional satellite drag models.

David Johnson's PhD thesis has been carried out under the supervision of Dr Aruliah and Prof Alan Aylward at UCL, and Prof David Jackson at the UK Meteorological Office. He has been applying a data assimilation technique known as Newtonian relaxation (e.g Telford et al. 2008), with CMAT2. Data assimilation is fairly new to upper atmosphere modelling, though well used for meteorological weather modelling. David Johnson has used the ECMWF ERA-I reanalysis (e.g. Dee et al., 2011) which spans the ground to the stratopause (~50 km), and the NRL NOGAPS-ALPHA reanalysis data which covers altitudes up to the bottom of the thermosphere at around 80 km (e.g. Hoppel et al., 2008). The relaxation 'nudges' CMAT2 prognostic variables towards those of the reanalysis in order to drive lower and middle atmosphere circulation and temperature.

The influence of migrating and non-migrating tides on the vertical propagation of energy and momentum is an area of active research at present. Of particular interest has been the effect of the low latitude forcing linked to thermospheric and ionospheric variability, primarily through low latitude **E** x **B** drift (e.g. England, 2011). However dramatic perturbations to thermosphere and ionosphere properties have also been observed in high altitude polar regions, both during quiet time solstice conditions, and during sudden stratospheric warming events (e.g. Akmaev, 2011), which is clearly of interest to this study.

As neutral density in CMAT2 is calculated using the ideal gas law, perturbations to winds and temperature will also indirectly influence density. Therefore we can use a suite of CMAT2 simulations to disentangle different contributions to large scale density structures, for example from Joule heating (using SuperDARN electric field patterns), forcing from below using relaxation and parameterised tidal modes, and arbitrary heating sources such as our 3rd upwelling study funded by the USAF. David Johnson was funded in this study to simulate upwelling in the midnight auroral region using CMAT2, and so provides vital experience of both the model and this type of study. The original proposed goals were to prepare a set of CMAT2 simulations along the following procedure:

a) with and without tides;
b) with and without data assimilation
c) add a simulation of the auroral heating source observed by the FPI-SuperDARN measurements of Joule heating, and determine the effect on thermospheric density, in particular identifying tidal modes.
d) prepare a set of CMAT2 simulations to be used to identify the magnitude of satellite perturbations from persistent meso-scale structures

2.5 QB50 mission initial results from the Phoenix CubeSat Ion Neutral Mass Spectrometer

The QB50 mission allows us to look ahead to the potential of CubeSat measurements as low-cost "weather balloons" providing regular in-situ measurements of upper atmospheric conditions. QB50 was a €8M mission funded by the EU (https://www.qb50.eu/). Realtime plots of the orbits may be seen at the link https://upload.qb50.eu/. Only 36 of the original 50 international student-built CubeSats made it through the rigorous selection procedures for space readiness, 28 were deployed

from the ISS (altitude 415 km, inclination 51.6°); and 8 were launched by rocket into near polar orbits (altitude 475 km). Each CubeSat carried one of three key sensors measuring particle densities (Ion Neutral Mass Spectrometer INMS, Flux Probe Experiment FIPEX and Multi-Needle Langmuir Probe MNLP, Thoemel et al., 2014). The UCL Mullard Space Science Laboratory (MSSL) designed and built the 11 miniaturised INMS (220g mass!), plus UCLSat to carry one INMS. QB50 was a technology demonstrator experiment, and we do not yet know the lowest altitude for observations. However, it shows the future possibilities for an altitude region from 90-300 km that is very poorly understood owing to a severe lack of measurements. Currently the modified Bates temperature profile (a simple exponential term plus a constant, defined by the temperatures at the exobase and at 120km) suffices for satellite drag density models (Bruinsma et al., 2003). Comparison of CMAT2 compositions with QB50 measurements will help validate the spectrometer.

3. Results and Discussion

Vertical winds have become an important consideration over recent years. Note that nearly all models of the thermosphere assume hydrostatic equilibrium, including our own CMAT2. There are only two non-hydrostatic models of the thermosphere: the global ionosphere-thermosphere model GTIM (Ridley et al., 2006) and the Upper Atmosphere Model (UAM) (e.g. Förster et al., 1999). The hydrostatic models simplify the equations of motion by assuming that buoyancy balances gravity. So by ignoring vertical motion, these models suppress vertical winds to a global average of less than 1-3 ms^{-1}. This is consistent with observations for middle and low latitude motion which dominated early observations of the upper atmosphere in the 1970s-1980s. Yet, in later years, as photon detector sensitivity improved rapidly and exposure times could be reduced, FPI observations at high latitudes have shown large vertical winds of a few 10's ms^{-1}, both upward and downward, associated with the energetics of the auroral oval (e.g. Price and Jacka, 1991). However, these large vertical winds are still a point of contention, and require careful scrutiny, as will be discussed below.

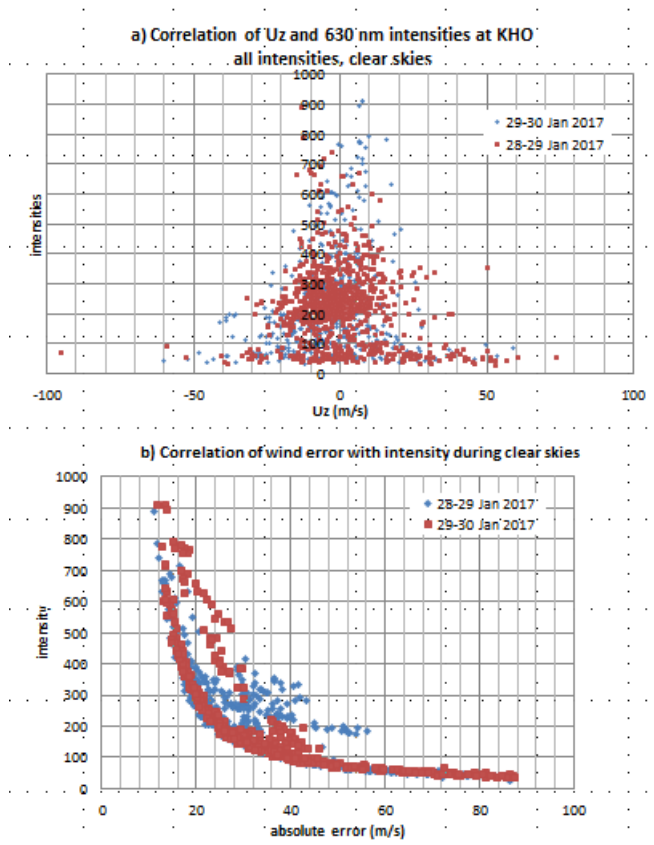

Figure 7 a) the correlation of vertical winds (Uz) and the 630 nm intensities at Longyearbyen are shown using as an example the clear sky periods during the nights of 28-29 and 29-30 January 2017. A cutoff of intensities < 50 should remove all OH contamination.

3.1 Sensitivity of FPI vertical wind measurements on 630 nm intensity, cloud and OH contamination

Vertical winds in the thermosphere are generally around 2 orders of magnitude smaller than horizontal winds. Cloud scatter of Doppler shifted photons can contaminate FPI measurements to the zenith, hence the need for cloud monitoring from all-sky cameras, and the recently installed Cloud Sensors described in section 2.2. The case studies presented here have had cloudy periods removed.

Further consideration is also given to the dependence of wind error on the signal to noise of the 630 nm emission intensity, and the consequence for the precision of vertical wind measurements. Figure 7 shows observations by the Longyearbyen FPI on two consecutive nights: 28-29 (red squares) and 29-30 January 2017 (blue diamonds). Figure 7a) shows the correlation of the vertical winds Uz and the 630 nm intensities, and 7b) the correlation of the wind error with intensity. These show that below an intensity count of 100 there was a wide range of vertical wind values between -95 to +74 ms^{-1}; and also the wind uncertainty can be as large as ±90 ms^{-1}. Table 1 shows the median, standard deviation, maximum and minimum vertical wind observed, when the cloudy periods identified by the cloud sensor have been removed. The data were then selected for intensities were greater than 50, 100, 200 or 300 counts. By increasing the intensity threshold, the median Uz approaches zero and the standard deviation reduces to between 6-10 ms^{-1}. This does not necessarily mean that the lower intensity measurements of large vertical winds are unreliable. A median vertical wind close to zero is consistent with an atmosphere in hydrostatic equilibrium, however, the standard deviation is far larger than what a hydrostatic model would allow. Note also that large vertical winds were still seen at higher intensity thresholds. For intensities greater than 300 counts, the maximum and minimum winds were up to 75 ms^{-1} during the substorm period.

Table 1 Three case studies showing the range of vertical wind measurements when the intensity of the 630 nm emission is taken into consideration

26-27 Jan 2017	median Uz	stdev Uz	max Uz	min Uz
clear sky periods and all intensities	-6.1	28.2	133.6	-112.0
> 50 counts	-6.7	24.6	104.7	-73.5
> 100 counts	-7.3	20.4	63.9	-73.5
> 200 counts	-8.7	17.3	33.0	-73.5
> 300 counts	-9.1	18.2	33.0	-73.5
28-29 Jan 2017	median Uz	stdev Uz	max Uz	min Uz
clear sky periods and all intensities	-1.8	15.0	73.7	-95.1
> 50 counts	-1.9	13.9	73.7	-95.1
> 100 counts	-2.4	10.5	50.0	-31.7
> 200 counts	-1.9	9.9	50.0	-31.7
> 300 counts	0.6	10.3	50.0	-18.4
29-30 Jan 2017	median Uz	stdev Uz	max Uz	min Uz
clear sky periods and all intensities	-3.0	15.6	58.8	-60.2
> 50 counts	-3.0	14.4	58.8	-48.3
> 100 counts	-2.9	12.1	27.6	-40.9
> 200 counts	0.1	9.1	26.7	-25.6
> 300 counts	1.4	8.2	25.4	-22.8

Ronksley (2016) recently identified two OH emission lines at 629.77 nm and 630.68 nm potential contaminations of the 630.0 nm emission. The FPIs have a filter positioned between the etalon and

camera. The filter has a 1 nm bandwidth that is centred at 630.2 nm for on-axis rays and 629.8 nm for rays at the edge of the beam at 629.8 nm. Thus the filter allows these OH emission lines through, but they are weak: 5-8 R for the $P_1(3)$ line and 2-4 R for the $P_2(3)$ line (Hernandez, 1974). Figure 8 shows her simulation of the spectrograph contamination of the 630 nm emission (black) by the nearby OH emissions at 629.77 nm (blue) and 630.68 nm (green). Here the 630 nm emission is set to be a weak 10 R with zero Doppler shift, centred at bin 54, while the OH emissions are 2 R, centred at bins 46 and 103, respectively. The red line is the sum of the intensities. Consequently there is an apparent shift to a lower bin value, equivalent to a red Doppler shift where there should be none.

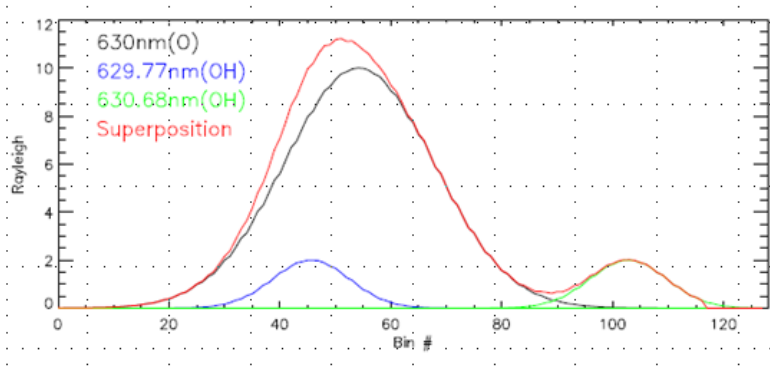

Figure 8 Figure from Ronksley (2016) to show a simulation of the spectrograph when there is contamination of the 630 nm emission (black) by the nearby OH emissions at 629.77 nm (blue) and 630.68 nm (green). Here the 630 nm emission is a weak 10 R, centred at bin 54, and the OH emissions are 2 R, centred at bins 46 and 103, respectively. The red line is the sum of the intensities.

The OH lines arise from a layer in the mesopause at ~ 87 km altitude (Dryland, 2013), so the Doppler shifts and Doppler broadening from winds and temperatures are significantly smaller than those of the auroral region upper thermosphere (above 200 km). Mesopause vertical winds are in the region of 0-2 ms^{-1} and winter mesosphere temperatures of 200 K. This compares with the auroral upper thermosphere vertical winds of 10s ms^{-1} and winter temperatures greater than 700 K. Thus Ronksley found that the OH contamination only became significant when the 630 nm emission dropped below 50 R. The FPIs are not normally calibrated for intensity, but for her PhD thesis, Ronksley calibrated the Longyearbyen FPI for December 2007 with the co-located Meridional Scanning Photometer. This gives us a reasonable method to calibrate counts and allows us to decide where a suitable cut-off should be for OH contamination when investigating the vertical winds.

3.2 Case study 1: 26-27 January 2017 geomagnetic substorm conditions

A case study from the night of 26-27 January 2017 was identified when there were clear skies and examples of sustained up/downwelling were observed by the Longyearbyen FPI observing the zenith direction at high time resolution. This was a geomagnetically disturbed night with Kp values between 3o to 4+ throughout. Figure 9a shows 3 periods of significant and sustained up/downwelling between 02-04 UT on 27 January 2017. These are upwelling during 01.46-01.62UT; upwelling during 01.96-02.57 UT; and downwelling during 03.12-03.57 UT (Table 2 shows a further analysis of these periods, which is discussed later). The duration of up/downwelling vertical winds range from 7-20 minutes. The average error bars are large (~ ±45 ms^{-1}) because the 630 nm intensities are low, and several overlap the zero line, thus convention would have it that the vertical wind could be zero. However, we have set up a high time resolution monitoring sequence for vertical winds, where there are 4 consecutive zenith observations (each exposure 30 seconds), interspersed by 2 or 3 look directions towards the horizontal directions, and the calibration lamp (i.e. a sequence of 4 x zenith, north-west, calibration lamp, south-west, 4 x zenith, south-east, north-east). The complete sequence takes about 6.5 minutes. Thus the trend is as important as the error bar in determining the accuracy of

the vertical wind measurement. If there is only a single large vertical wind measurement, then it is not reliable, but we can see clear trends in the vertical winds shown in Figure 12a.

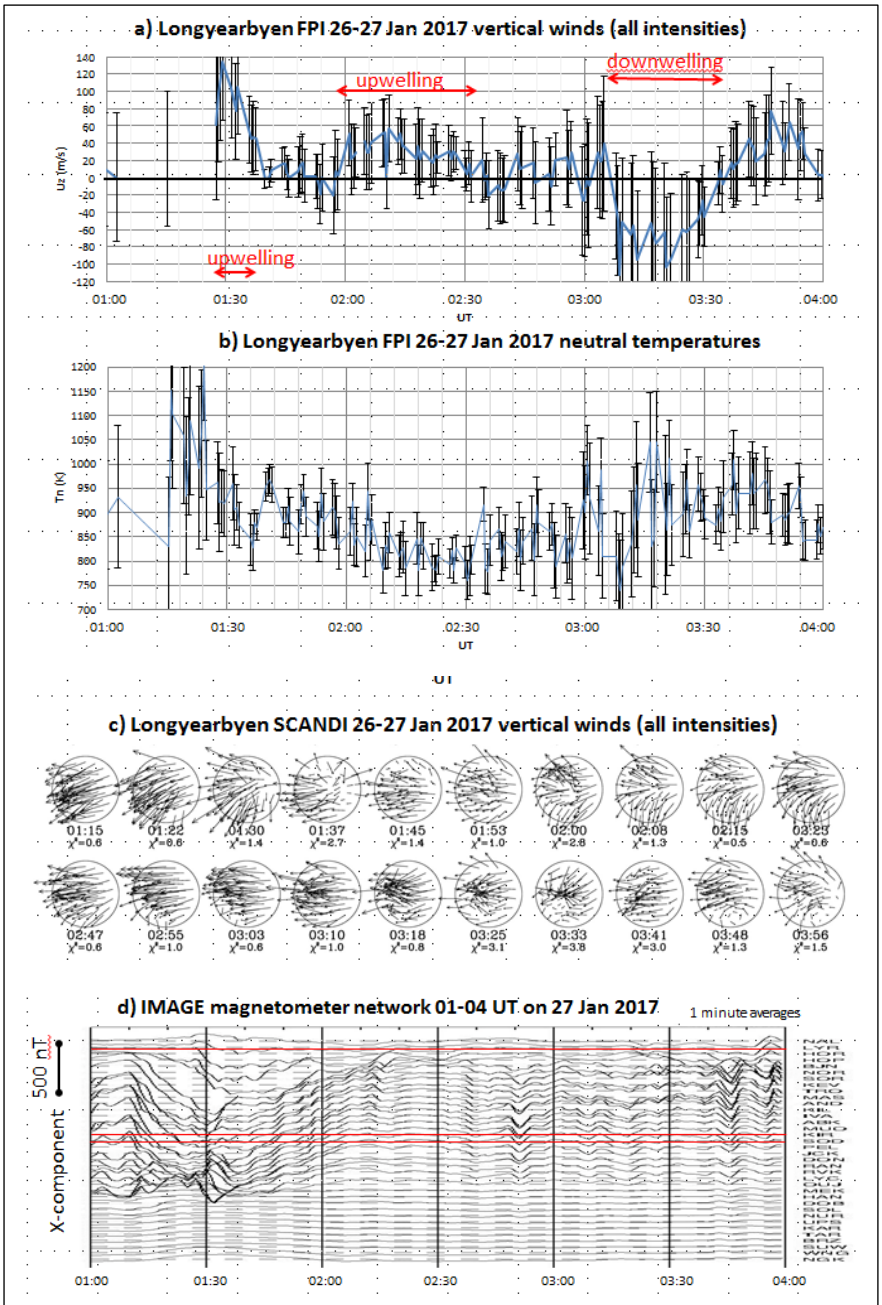

Figure 9 Observations from Longyearbyen for the period 01:00-04:00 UT on the night of 26-27 January 2017 are presented here. This was a geomagnetically active period with Kp = 4+. FPI measurements of a) vertical neutral winds and b) neutral temperatures at 240 km altitude; c) SCANDI horizontal wind field for a diameter of ~1000 km at 240 km altitude; and d) IMAGE magnetometer chain measurements of the perturbation of the x-component of the Earth's magnetic field, which indicates the latitudes covered by the auroral currents in the ionosphere.

Upwelling occurs above the heating source, where the heated gas rises, and then falls on either side of the source. Figure 9b shows the neutral temperatures determined from the Doppler broadening of the FPI intensity peaks. They range between 738-995 K with an average error ± 60 K and standard deviation of ± 60 K. There is a surprisingly poor correlation between the vertical winds and neutral temperatures (during clear periods R^2=0.0005 for the whole night 0.0001 for 01-04UT. The expectation is that the up/downwelling should be represented by an increase/decrease in neutral temperature. Figure 9c shows the wide field observations of the horizontal component of the neutral winds observed by SCANDI. The SCANDI horizontal wind field shows corroboration of the FPI vertical winds from an independent instrument. We see classic signatures of diverging winds at around 01:30 UT and 02:00 – 02:30 UT as expected during upwelling, and converging winds between 03:00 - 03:30 UT as expected for downwelling seen by the FPI.

The 3-hourly Kp values for 00-06 UT on 27 January 2017 were 4+ 4+. The corresponding magnetic perturbations observations by the IMAGE magnetometer chain (e.g. Tanskanen, 2009) are shown as stacked plots according to the latitude of the site in Figure 9d. Red lines indicate the baselines for Longyearbyen, Kiruna and Sodankylä. These perturbations are caused by electrical currents flowing in the ionosphere. The x-component is a good indication of the

location in latitude, and east-west direction, of ionospheric currents that cause Joule heating. The geomagnetic Kp index is 4^+ between 00-06 UT, which is moderately strong level of geomagnetic activity. It is clear that the ionospheric currents move poleward, from south of Longyearbyen to near overhead by 05 UT.

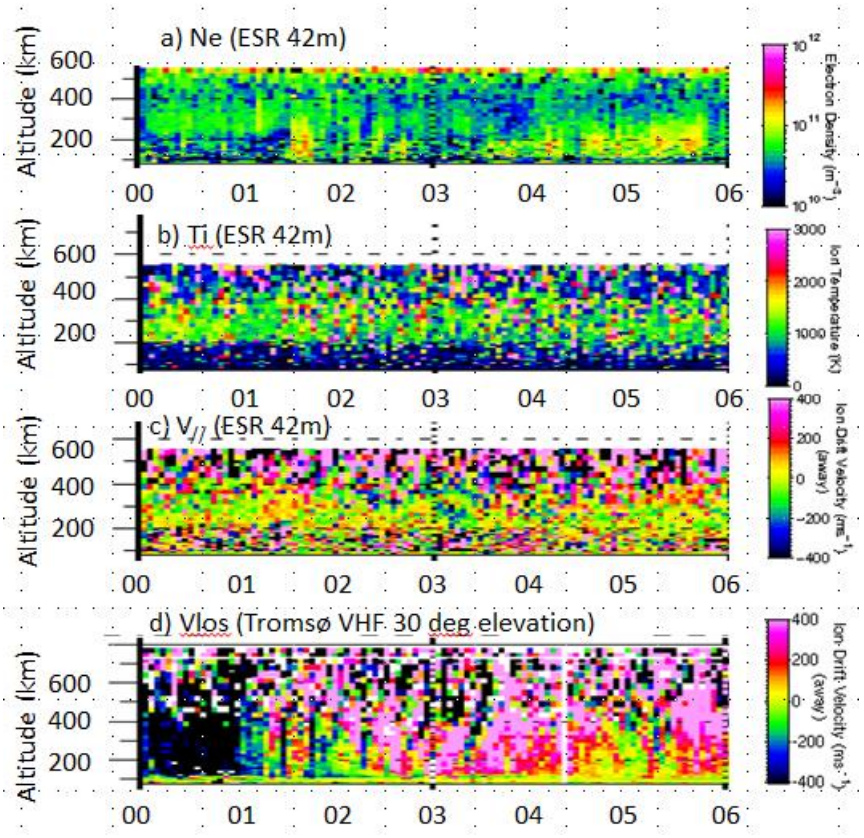

Figure 10 The 42m magnetic field-aligned dish of the EISCAT Svalbard Radar measurements of the height distribution of ionospheric parameters are shown here for the period 00-06 UT on 27 January 2017. a) electron densities; b) ion temperatures and c) the line-of-sight component of the plasma speed along the magnetic field $V_{//}$; and d) the Tromsø VHF radar line-of-sight plasma velocities pointing northward, with elevation 30°.

Figure 10 shows the 42m EISCAT Svalbard Radar measurements along the Earth's magnetic field line *B*. The radar pointing direction is azimuth = -175.5°, elevation = 81.6°. The figure shows the height distributions for 00-06UT on 27 January 2017 for a) electron densities; b) ion temperatures; c) the line-of-sight component of the plasma speed along the B-field.; and d) the Tromsø VHF radar line-of-sight component of the plasma speed at elevation= 30° pointing to the geographic North. Although the Kp value is 4^+ during the whole period 00-06 UT, the ionospheric parameters are more typical of a quiet period, with low background electron densities up to 10^{11} m^{-3}. It should be noted that the monthly f10.7 solar flux level for January 2017 is 75, which is near the lowest values observed in the solar cycle. The period of upwelling between 01.46-01.62 UT happened during a period of soft particle precipitation peaking around 200 km altitude. There was no similarly clear precipitation to account for the 2nd period of upwelling (01.96-02.57 UT). The third period (03.12-03.57 UT) was a downwelling, which was accompanied by a reduced electron density compared with earlier and later times.

There was no particularly clear pattern of variation in the ion temperatures. However, examination of the field-parallel plasma speeds $V_{//}$ when compared with the vertical winds U_z (Figure 11) shows a strong correlation. The ESR 1-minute $V_{//}$ were linearly interpolated to the same times as the FPI U_z. This is a classic demonstration of the momentum equation, which in its simplified form is given by equation 1 (e.g. Schunk, 1975; Winser et al., 1988). The consequence of the conservation of momentum is that the neutral winds drive plasma up or down a field line, as demonstrated in Figure

11. The plasma speeds also provide strong independent evidence confirming that these large FPI observed vertical winds are real.

$$\underline{V}_{//} = \underline{U}_{//} + W_d \tag{1}$$

Where W_d is the ambipolar diffusion given by equation 2, ν_{in} is the ion-neutral collision frequency, m_i is the ion mass, $\underline{g}$ is gravitational acceleration and I is the inclination of the magnetic field. the calculation is based on the gradient with respect to height h of the gravitational and plasma pressure forces.

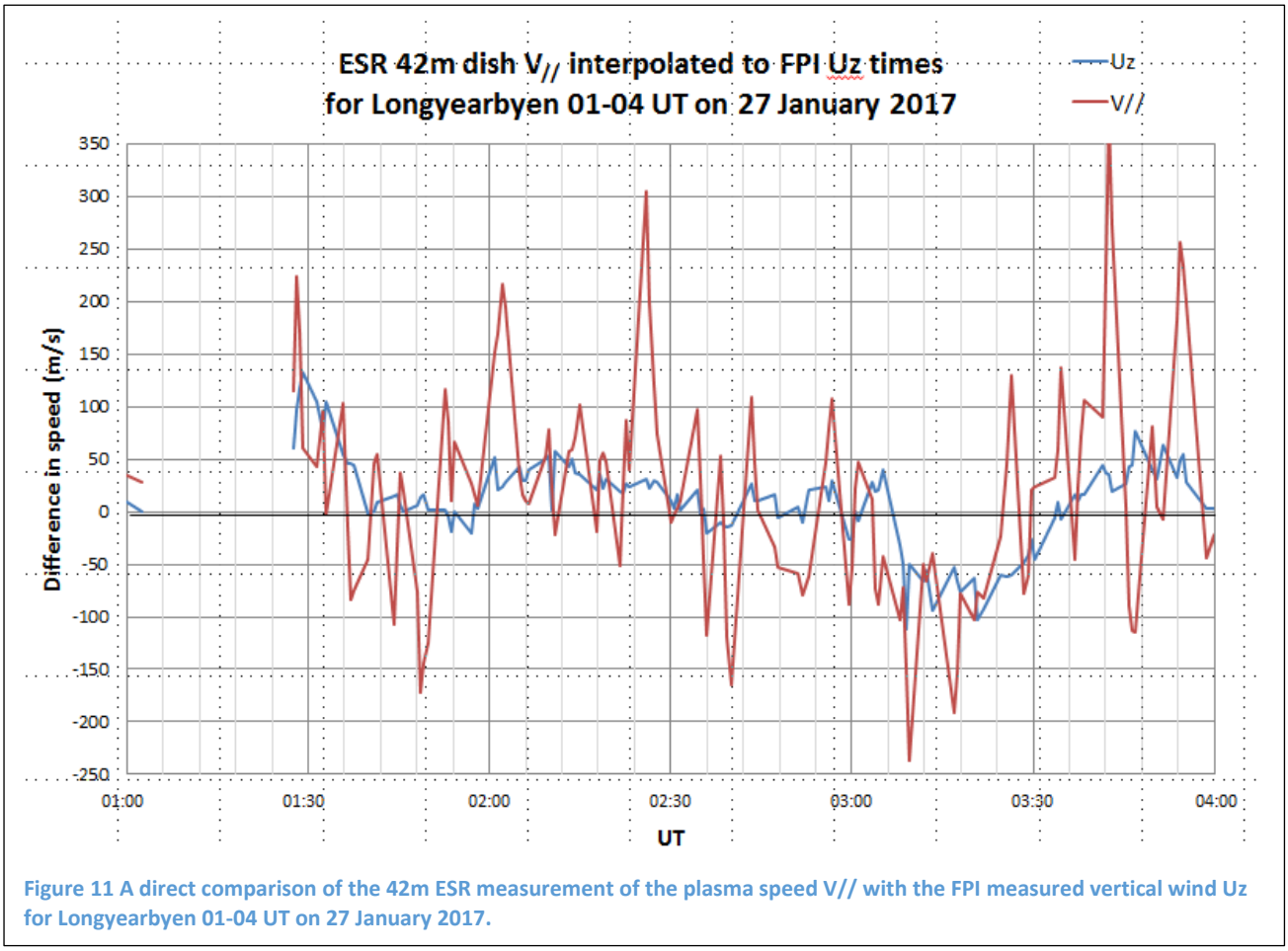

Figure 11 A direct comparison of the 42m ESR measurement of the plasma speed V// with the FPI measured vertical wind Uz for Longyearbyen 01-04 UT on 27 January 2017.

$$W_d = -\frac{\sin I}{\nu_{in}}\left\{\underline{g} + \frac{k}{m_i N_e}\frac{\partial}{\partial h}\left[N_e(T_i + T_e)\right]\right\} \tag{2}$$

The simplified momentum equation can be rearranged to determine the neutral density n_n from radar measurements of the ionosphere (equation 3) as shown by e.g. Vickers et al. (2013). Here T_{in} is the average of the ion and neutral temperatures.

$$n_n = \frac{\nu_{in}}{3.67\times10^{-11}\sqrt{T_{in}}\,(1-0.064\log_{10}T_{in})^2} \tag{3}$$

We have used this procedure to estimate the neutral density for the period used in Case 1, which is shown in a height versus time plot in Figure 12a. There is no indication of the up/downwelling from

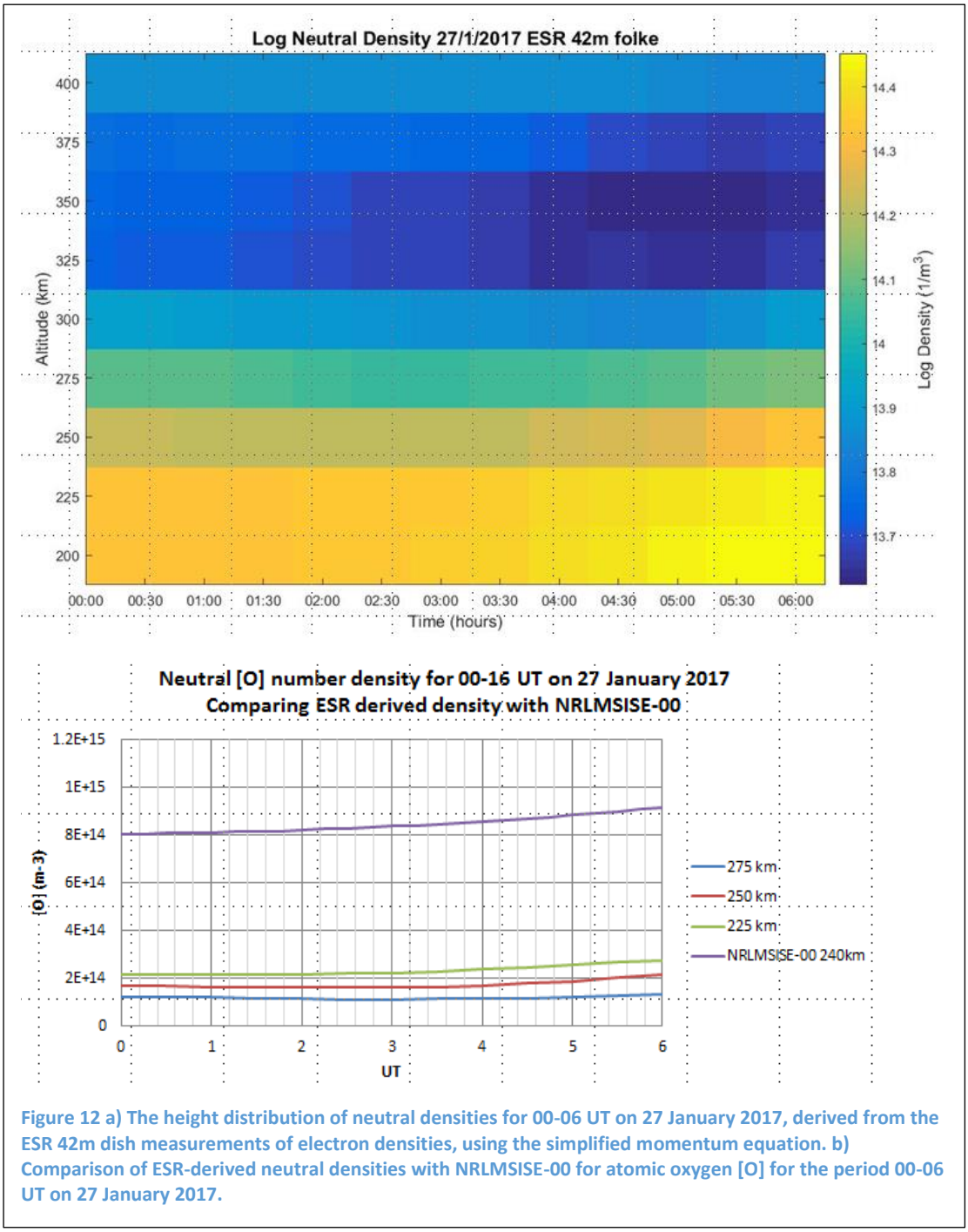

Figure 12 a) The height distribution of neutral densities for 00-06 UT on 27 January 2017, derived from the ESR 42m dish measurements of electron densities, using the simplified momentum equation. b) Comparison of ESR-derived neutral densities with NRLMSISE-00 for atomic oxygen [O] for the period 00-06 UT on 27 January 2017.

these calculations. This is seen more clearly in the line plots in Figure 12b, where the densities at 225, 250 and 275 km altitude are plotted, and are shown to be smoothly varying over this 6 hour period (00-06 UT). Addition of the NRLMSISE-00 (Picone et al., 2002) semi-empirical model of density for 240 km shows that the estimate of densities from the ESR 42m dish are within the expected magnitude, but the model densities are also smoothly varying, despite the substorm Kp indices, and are nearly 5 times larger on average. This indicates the limitations of large-scale spherical harmonic models in capturing mesoscale structures, which are typical during substorms at auroral latitudes.

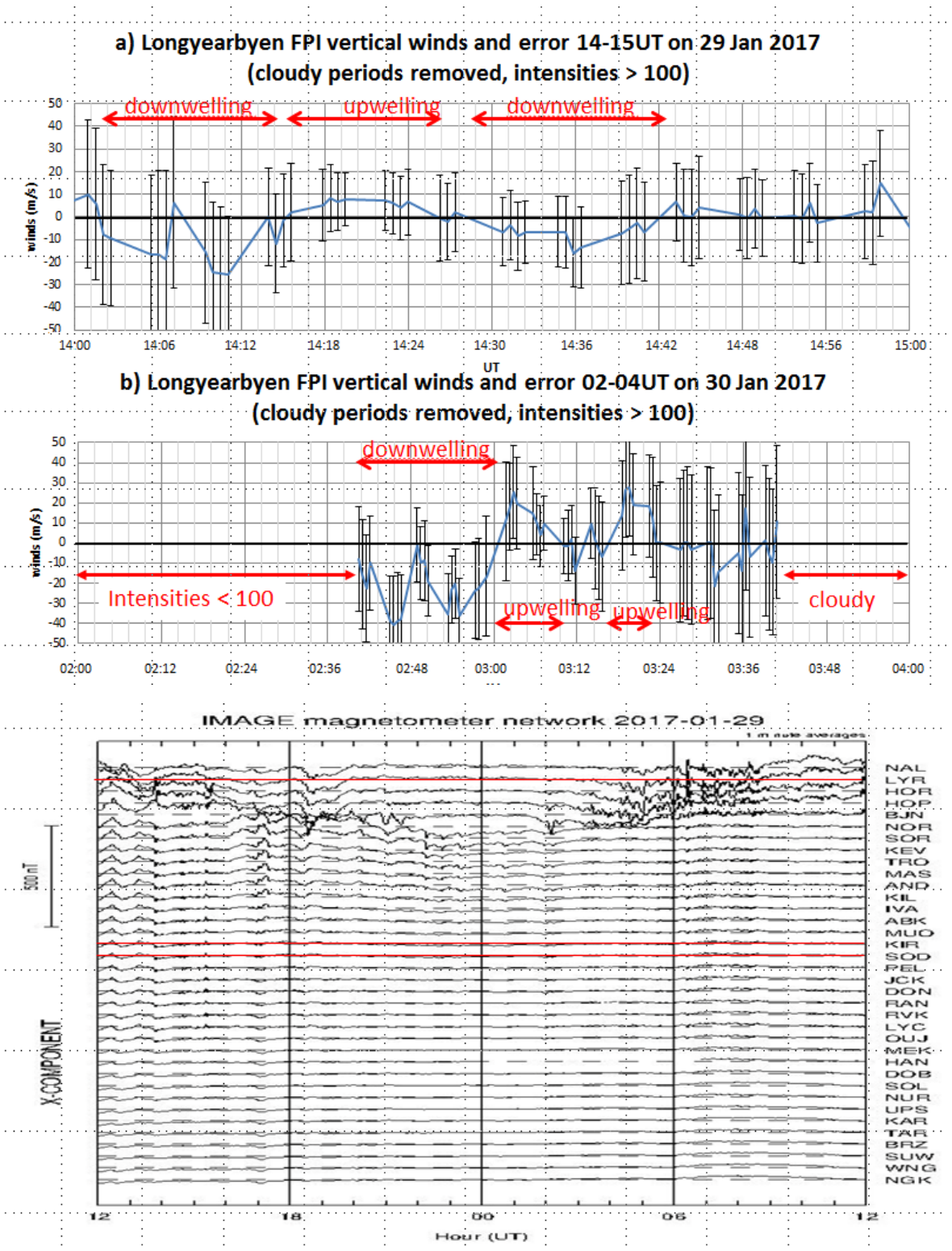

Figure 13 FPI observations from Longyearbyen for the periods 14:00-15:00 UT and 02:00-04:00 UT on the night of 29-30 January 2017 are presented here. Cloudy periods have been removed. This was a geomagnetically quiet period with Kp = 2- and 1o, respectively, as indicated by the smaller perturbations of the x=component of the Earth's magnetic field shown in c) IMAGE magnetometer chain measurements for the night of 29-30 January 2017.

3.3 Case Study 2: 29-30 January 2017 post substorm, quiet conditions

Figure 13 shows vertical winds measured during the night of 29-30 January 2017 when there were clear skies, and large and sustained vertical winds. Several periods have been identified, which show vertical winds up to 40 ms^{-1} in magnitude. The error bars vary between ±15-40 ms-1 according to the

intensities, but the trends are clearly shown by the use of high time resolution FPI vertical measurements. The corresponding magnetic perturbations observations by the IMAGE magnetometer chain are shown in Figure 13c. The remnants of the substorm from 26 January 2017 are seen in the weak, but significant magnetic perturbations, which were largely confined to the polar cap region where Longyearbyen is located. The ionospheric currents moved equatorward towards Tromsø around 22 UT, and then retreated poleward again to be overheard of Longyearbyen by 06 UT. Despite the relatively quiet conditions, sizeable vertical winds up to nearly 40 ms^{-1} downwards were observed by the Longyearbyen FPI. Figure 13a shows the afternoon period 14-15UT when there was a down-welling occurring between 14-14.3 UT, reaching a maximum of 25 ms^{-1}; and also for Figure 13b, where a strong downwelling occurred between 02.4-03.0 UT on 30 January 2017.

Figure 14 shows the ESR 42m dish ionospheric measurements for the period 14-15 UT on 29 January 2017: a) electron densities; b) ion temperatures and c) field-parallel plasma flow speed. On inspection of the electron densities between 14-15 UT, it can be seen that there was a clear upwelling for the FPI vertical winds at the same time as the particle precipitation, with downwelling before and after. Figure 10c shows that the Bx perturbations caused by overhead ionospheric currents were over Longyearbyen during the period 14-15 UT, but these currents had travelled from the north before 14

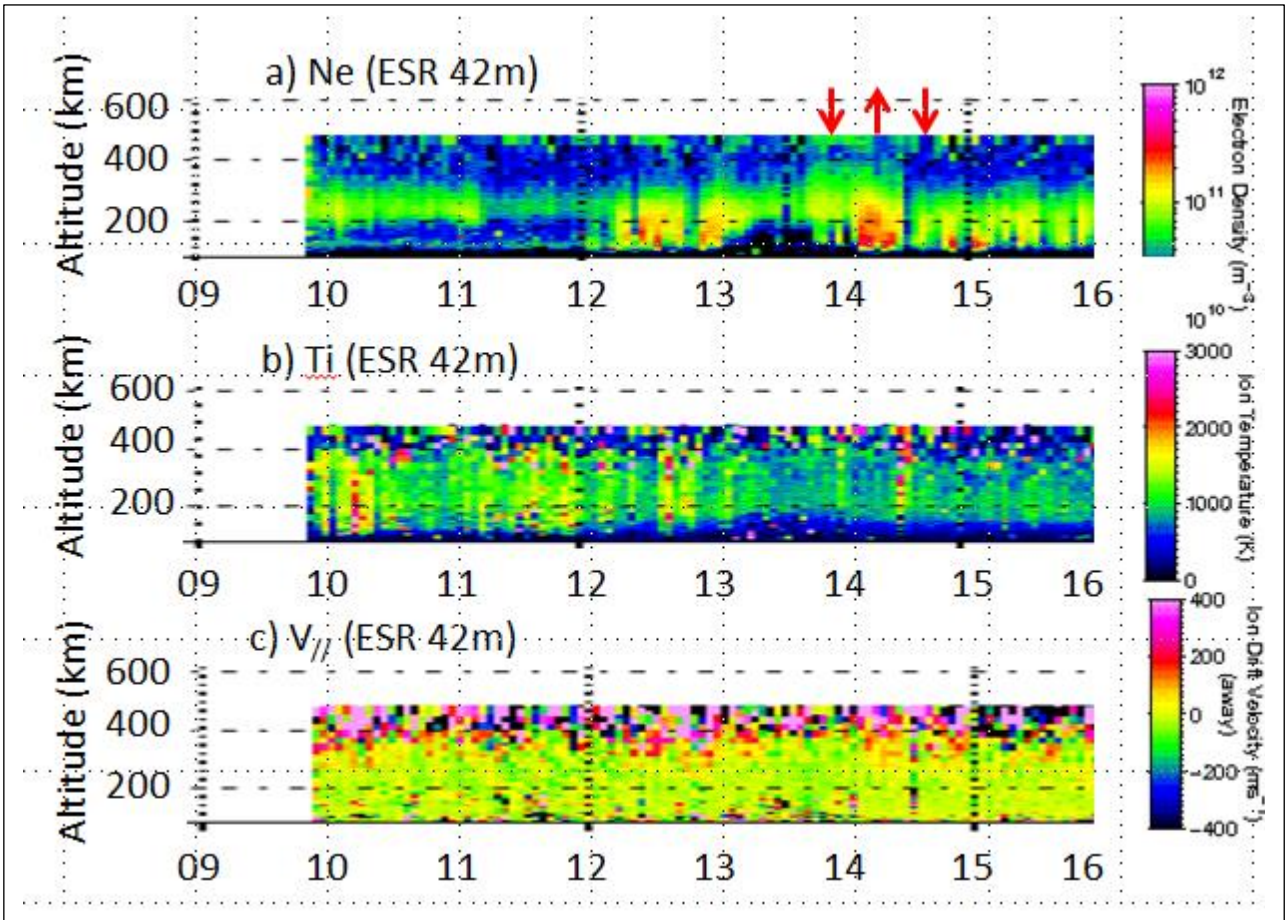

Figure 14 The 42m magnetic field-aligned dish of the EISCAT Svalbard Radar measurements of the height distribution of ionospheric parameters are shown here for the period 14-15 UT on 29 January 2017. a) electron densities; b) ion temperatures and c) the line-of-sight component of the plasma speed $V_{//}$.

UT and were heading south after 15 UT. The FPI observations could be interpreted as the site passing through a convection cell and seeing the downwelling on either side of the upwelling above the heating region.

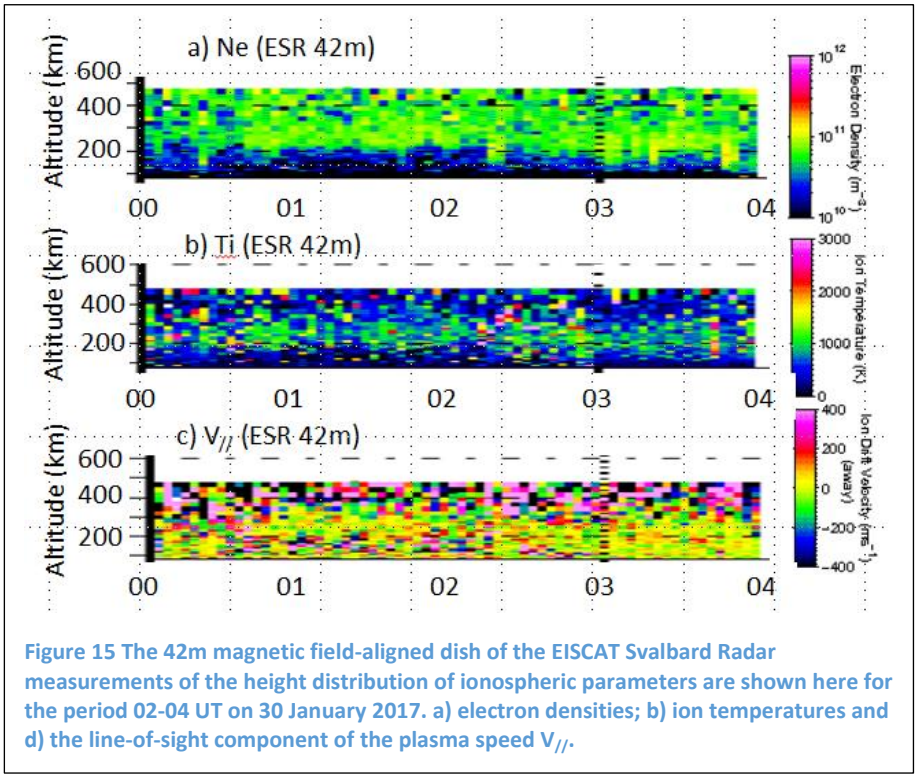

Figure 15 The 42m magnetic field-aligned dish of the EISCAT Svalbard Radar measurements of the height distribution of ionospheric parameters are shown here for the period 02-04 UT on 30 January 2017. a) electron densities; b) ion temperatures and d) the line-of-sight component of the plasma speed $V_{//}$.

Figure 15 shows the ESR 42m dish ionospheric measurements for the morning hours of this night i.e. the period 02-04 UT on 30 January 2017. The electron densities were low (5-10x10^{11} m^3) and there was no particle precipitation during this period.

Figure 16 shows the FPI vertical winds U_z compared with the interpolated ESR 42m dish field-aligned plasma speed $V_{//}$ for an extended time around the two periods: a) 13-16 UT on 29 January 2017 and b) 00-14 UT on 30 January 2017.

The clear correlation between U_z and $V_{//}$ that was seen on the substorm night is not so apparent here, though some hint of a trend seems possible in the period 14-15 UT when particle precipitation would have increased the electron densities by an order of magnitude, and thereby the ion-neutral coupling.

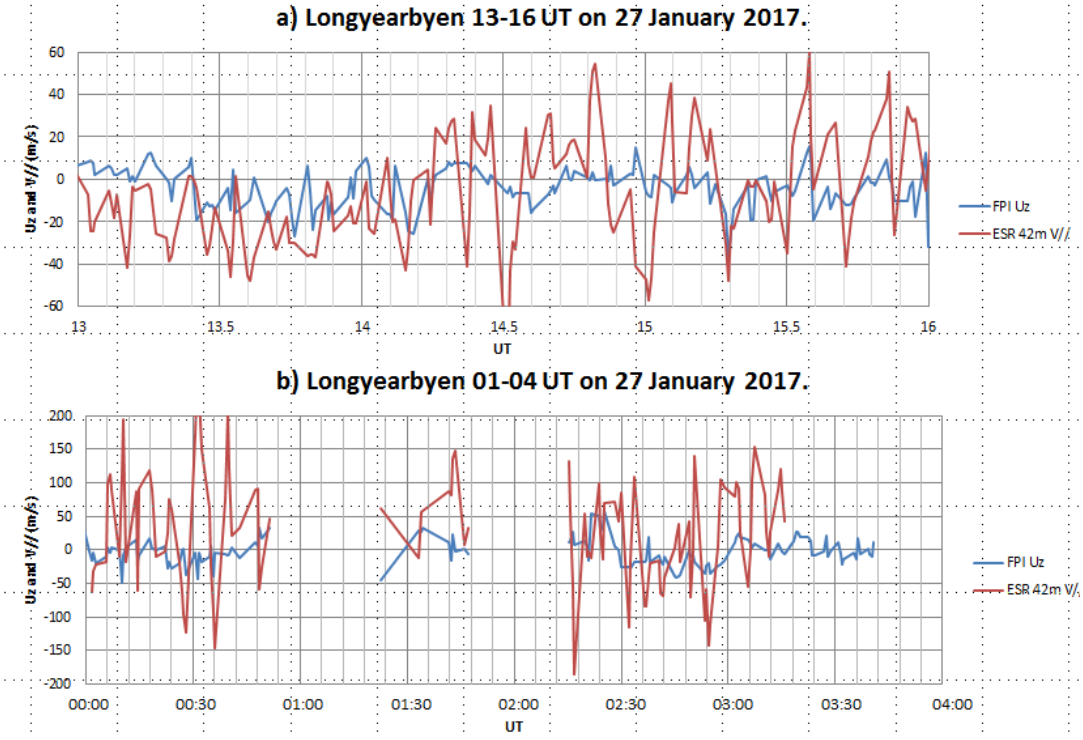

Figure 16 A direct comparison of the 42m ESR measurement of the plasma speed V// interpolated to the FPI measured vertical wind Uz for Longyearbyen at a) 13-16 UT and b) 01-04 UT on 27 January 2017.

3.4 Estimating energy involved in up/downwelling

Having shown evidence of significantly large and sustained up/downwelling, during both active and quiet geomagnetic conditions, it can be estimated what quantities of energy are required to sustain this vertical motion. If it is assumed that the Earth is rotating under a fixed Sun-aligned pattern of heating, such as Poynting flux energy, then the horizontal extent of the heating region may be determined from the duration t of the up/downwelling from the angular/longitudinal distance $\phi = \omega t$, or $s = vt$, where ω and v are the angular or rotational speed respectively. The rate of change of potential energy dQ/dt to lift the volume of gas above the heating region is determined from the average vertical wind Uz (= dz/dt) during the period, multiplied by the mass m and gravity g.

$$\frac{dQ}{dt} = mg\frac{dz}{dt} \tag{4}$$

Energy estimates were calculated using the average mass density from the NRLMSISE00 web model (https://ccmc.gsfc.nasa.gov/modelweb/models/nrlmsise00.php). A summary of the average values in example periods of up/downwelling are given in Tables 2-4.

Calculations of the rate of change of potential energy represented by the observed vertical winds for Case 1, which was a geomagnetically active night, are given in Table 2. For 02-04 UT on the 27 January 2017 (Table 2) the rate of change of potential energy required to lift a column above 120 km altitude is of the order of $2x10^{-1}$ Wm^{-3}, but only around $1x10^{-3}$ Wm^{-3} to raise a column above 180 km altitude. The same set of calculations were done for Case 2, which was a quiet night; and are given in Tables 3 and 4. In our calculations, for 14-15 UT on the 29 January 2017 (Table 3) the rate of change of potential energy required to lift a column above 120 km altitude is of the order of $1x10^{-2}$ Wm^{-3}, but only around $1x10^{-4}$ Wm^{-3} to raise a column above 180 km altitude. For 02-04 UT on the 30 January 2017 (Table 4) the rate of change of potential energy required to lift a column above 120 km altitude is of the order of 0.1 Wm^{-3}, but only around 10^{-4} -10^{-4} Wm^{-3} to raise a column above 180 km altitude. These values are also of similar orders of magnitude to those calculated using the non-hydrostatic GTIM model, e.g. Deng et al. (2012) who reported using total energy of 80 $x10^{-3}$ Wm^{-3} from a combination of soft precipitation and Poynting flux to achieve density changes of up to 60% at 400 km altitude. The vertical winds at 120 km altitude are smaller than at 240 km (i.e. the height of the FPI measurements), so the rate of change of potential energy calculated here is an upper estimate. The energy required to raise a column above 180 km is within the limits of the Poynting flux energy input for even geomagnetically quiet conditions shown in the model by Cosgrove et al (2014).

Table 2 Longyearbyen FPI 02-04 UT (Figure 9a) on 27 Jan 2017 (substorm)

duration for 25-28 UT on 26-27 Jan 2017 (substorm)	25.46 -25.62 UT (upwelling)	25.96- 26.57 UT (upwelling)	27.12 - 27.57 UT (downwelling)
Mean vertical speed during up/downwelling (ms^{-1})	80.7	27.8	-4.63
Duration of up/downwelling t (min)	9.6	36.6	27
Horizontal extent of up/downwelling region in longitude (deg)	2.4	9.15	6.75
Horizontal extent of up/downwelling region in distance *s* (km)	54.9	209	154
Average mass of column above 120 km altitude per m^2	3.80E-04	3.80E-04	3.80E-04
rate of change of Potential Energy (Wm^{-2}) to raise column ***above 120km***	3.01E-01	1.04E-01	-1.73E-02
Average mass of column above 180 km altitude per m^2	1.44E-05	1.44E-05	1.44E-05
rate of change of Potential Energy (Wm^{-2}) to raise column ***above 180km***	3.39E-04	1.29E-03	9.54E-04

Table 3 Longyearbyen FPI 14-15 UT on 29 Jan 2017 (Figure 10a) (quiet night, post-substorm)

Periods of interest: 14-15 UT on 29-30 Jan 2017	14.03-14.25 UT (downwelling)	14.26-14.40UT (upwelling)	14.44-14.74UT (downwelling)
Mean vertical speed during up/downwelling (ms^{-1})	-12.8	6.02	-4.63
Duration of up/downwelling *t* (min)	12	8.4	16.2
Horizontal extent of up/downwelling region in longitude (deg)	3	2.1	4.05
Horizontal extent of up/downwelling region in distance *s* (km)	68.6	48	92.6
Average mass of column above 120 km altitude per m^2	3.92E-04	3.92E-04	3.92E-04
rate of change of Potential Energy (Wm^{-2}) to raise column ***above 120km***	-4.92E-02	2.31E-02	-1.78E-02
Average mass of column above 180 km altitude per m^2	1.27E-05	1.27E-05	1.27E-05
rate of change of Potential Energy (Wm^{-2}) to raise column ***above180km***	3.75E-04	2.62E-04	5.06E-04

Table 4 Longyearbyen FPI 02-04 UT (Figure 10b) on 30 Jan 2017 (quiet night, post-substorm)

Periods of interest: 26-28 UT on 29-30 Jan 2017	26.67-27.0 UT (downwelling)	27.0-27.12 UT (upwelling)	27.31-27.38 UT (upwelling)
Mean vertical speed during up/downwelling (ms^{-1})	-22.6	13.9	19.7
Duration of up/downwelling *t* (min)	19.8	7.2	4.2
Horizontal extent of up/downwelling region in longitude (deg)	4.95	1.8	1.05
Horizontal extent of up/downwelling region in distance *s* (km)	113	41.2	24.0
Average mass of column above 120 km altitude per m^2	3.92E-04	3.92E-04	3.92E-04
rate of change of Potential Energy (Wm^{-2}) to raise column ***above 120km***	-8.69E-02	5.34E-02	7.57E-02
Average mass of column above 180 km altitude per m^2	1.27E-05	1.27E-05	1.27E-05
rate of change of Potential Energy (Wm^{-2}) to raise column ***above 180km***	6.19E-04	2.25E-04	1.31E-04

4. Effects of localised heating as simulated by a Global Circulation Model CMAT2

To investigate the vertical winds observed above Svalbard in January 2017, a suite of simulations were performed on the UCL Coupled Middle Atmosphere and Thermosphere (CMAT2) model. CMAT2 is a hydrostatic model, driven primarily by the F10.7 cm flux and Kp planetary indices, as well as forcing from below. Due to the hydrostatic equilibrium atmosphere assumption, momentum and energy calculations are performed with respect to a series of vertical pressure levels, as opposed to fixed height. As with other hydrostatic models, the result of this is that vertical motion and winds tend to be underestimated when compared to experimental data.

A control simulation was performed for the end of January 2017 using time-varying F10.7 and Kp indices to provide a baseline comparison to all experiments. When specifically investigating the early morning of the 27th January, the control simulation shows negligible vertical velocity (1-2ms^{-1}), even with the presence of moderate geomagnetic activity, and thus those results are omitted here.

Two subsequent experiments were performed to investigate upward propagating effects by:

a) driving the model additionally with lower boundary (15 km) diurnal and semi-diurnal tides using amplitudes and phases retrieved from the Global Scale Wave Model (GSWM),
b) implementing a relaxation/assimilation module to incorporate reanalysis in the lower atmosphere.

It was found that the use of tidal modes from GSWM did not perturb the neutral atmosphere above a height of approximately 110 km, and as a result the upper thermosphere remained relatively unchanged. The initial plan for the relaxation experiment was to use neutral velocities and temperatures extracted from the NRL NOGAPS alpha reanalysis, as this model spans troposphere – mesosphere/lower thermosphere altitudes, however unfortunately, as due to the experimental nature of this reanalysis project, January 2017 results were not available. Instead the ECMWF ERA-Interim reanalysis was used to drive the lower portion of the model (15-45 km) by relaxing to neutral velocities and temperature. Although this experiment perturbed the mesosphere/lower-thermosphere significantly, once again the upper thermosphere remained unchanged. This was not to be unexpected, due to the diurnal solar tide becoming the primary driver of the lower thermosphere (~100 km upwards) and effectively 'smoothing out' perturbations from below. Previously we had found that using the relaxation with the NOGAPS analysis did allow certain components to propagate to higher altitudes in the thermosphere, purely a result of forcing the model over a larger span of altitude, and this remains an active area of data assimilation research at UCL.

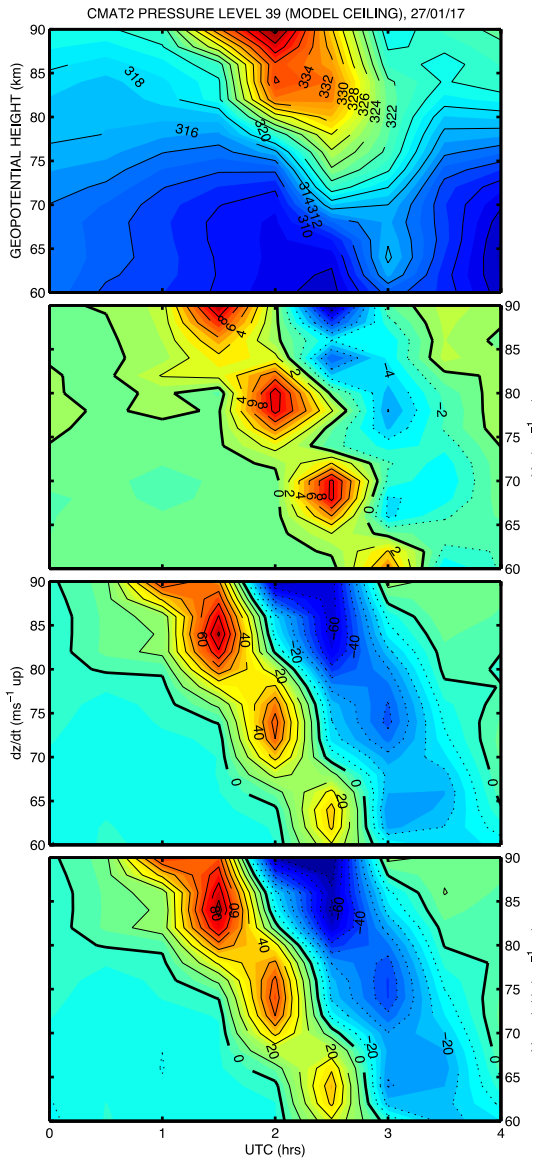

Figure 17 CMAT2 latitude versus time plots of the development of the top pressure level on 27 January 2017 at the Svalbard longitude (~18°E) after a localised heating event. a) Shows the height of the pressure level; b) vertical wind relative to the pressure level; c) rate of change of height of the pressure level; d) absolute vertical wind.

The final set of experiments performed included adding a module to insert an artificial heating event to a given region of the atmosphere. A similar experiment had been performed previously in the third EOARD-funded project, showing that a heating event inserted in the 150 km altitude region could simulate a soft particle precipitation event, and cause the local atmosphere to heat and expand. To simulate the activity seen on the morning of the 27th January 2017, a Chapman function was chosen, with a power of 3.0×10^{-9} GW, peaking at a pressure altitude of 4.0×10^{-4} Pa (approximately 145km). The latitude width of the heating source is represented by a Gaussian with sigma = 4°. This is meant to be representative of typical plasma flow channels as described in Carlson et al. (2012). The heating routine was run for one hour, with a ten minute warm up and cool down period on either side, centred at 0130 UT to correspond approximately to the events shown in Table 2.

Figure 17 shows the response of the top pressure level of CMAT2 to this heating event between 00-04 UT, over a large latitudinal range (60-90°N) at approximately Svalbard longitude (~18°E). The top graph shows the geopotential height response of the top pressure level to the heating event. It can be seen that there is a dramatic increase in geopotential height

in northern latitudes by up to 20km.

The second image shows the resultant vertical wind (ms^{-1} positive up) with respect to the pressure level. It can be seen that there is an upwelling/downwelling component to the vertical wind centred around the time of peak heating, to a magnitude of ± $9ms^{-1}$.

The third image is the time rate of change of the geopotential height shown in the first image. Using the Burnside et al. (1981) relation of summing the vertical wind w, relative to the pressure level p, and the time rate of change of pressure level height z_p, (equation 5) yields the fourth image, the absolute vertical wind U_z during this time. It can be seen that the resultant vertical wind is of similar magnitude to those observed at Svalbard at this time (see Table 1), with upwelling and downwelling velocities of approximately +/-90 ms^{-1}.

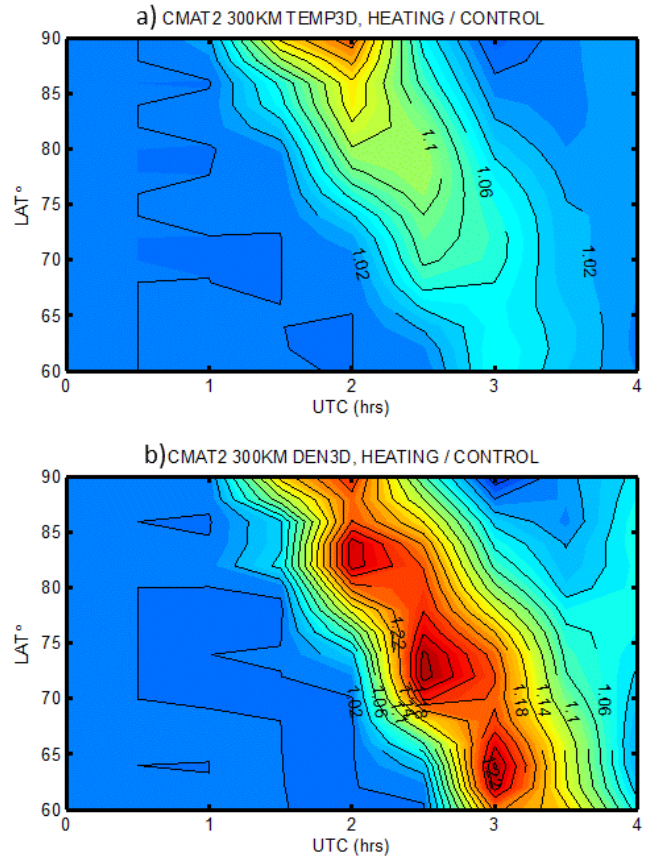

Figure 18 CMAT2 simulations at a fixed altitude of 300 km (similar to a satellite at fixed altitude) taking the ratio of the simulation of the heating event against a control without heating. a) Shows that the neutral temperature is raised by up to 20% in the polar regions during the upwelling. b) Shows the equivalent for the neutral density, which is over 20% larger during the heating event.

$$U_z = \frac{\partial z_p}{\partial t} + w \qquad (5)$$

The images in Figure 17 have been shown with respect to a fixed pressure level. Figure 18a shows a ratio between the experiment and control simulations of neutral temperatures. The neutral temperatures have been interpolated between pressure levels to a fixed height of 300 km. Under solar minimum conditions, the top of the CMAT2 thermosphere is only around 300 km, while LEO orbits are normally above 400 km. The aim is to represent a satellite orbiting at a fixed altitude. It can be seen that the neutral temperature at 300 km is raised by up to 20% in polar regions during the upwelling, with temperatures cooling down to ambient levels relatively soon after the event. The equivalent ratio for neutral density ratio is shown in Figure 18b. It is shown that neutral species are over 20% more abundant at 300 km during the heating event.

Figure 19 shows the geographic extent of the neutral density perturbation caused by the artificial heating event, interpolated onto a fixed geopotential height of 300km. The spatial range plotted is 70-90° N, 0-70° E.

It can be seen that a significant upwelling forms at this altitude during peak heating (approximately 2UT), with a peak density spanning 8 degrees in latitude (77°N – 85°N), and 55 degrees in longitude (0 – 55°E). However, it can also be seen that the ambient background atmosphere has also risen in density, when compared to 90 minutes, and 180 minutes after the heating has ended. The typical orbital period of a LEO satellite is around 90 minutes, and so three successive images are plotted:

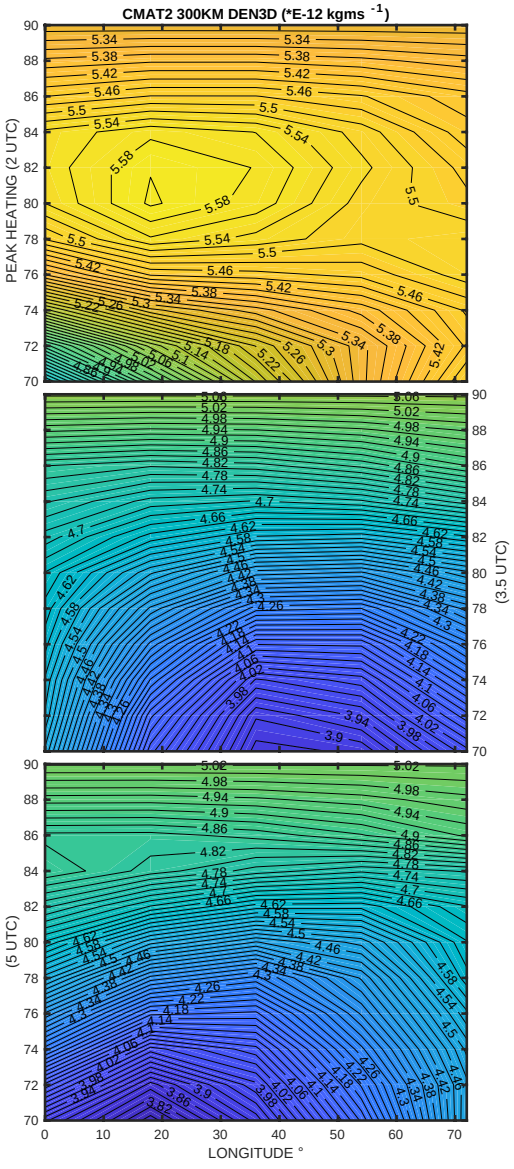

Figure 19 CMAT2 simulation showing the neutral density perturbation interpolated to a fixed height of 300km The middle and bottom figures show the same region 90 mins and 180 mins after the heating event.

top: at the time of heating, and the middle and bottom figures show the density perturbation at 90 and 180 mins afterwards. This type of simulation can be used to indicate what conditions a satellite faces during a geomagnetic storm/substorm.

What is also valuable about this simulation is the demonstration that it is possible to simulate meso-scale structures with a hydrostatic GCM. The motivation for the first EOARD project was to investigate the CHAMP observations of a doubling of density over the magnetic cusp. This was found to be very difficult to reproduce using a hydrostatic model. Demars and Schunk (2007) required energy levels 110 times larger than ever observed to achieve a doubling. Deng et al. (2013) were able to achieve density enhancements of up to 59% using more reasonable levels of heating with the non-hydrostatic Global Ionosphere-Thermosphere Model (GITM).

5. Preliminary Results from the QB50 CubeSat mission

The biggest problem for satellite missions is dealing with satellite drag. Orbit prediction relies on reliable modelling of satellite drag. Part of the problem is how realistic are atmospheric density models. The other part is how the satellite profile changes with respect to the atmosphere, and how gases interact with surface material. For precise, scientific mission work satellite engineers regard modelling errors at the level of nm/s^2 as large and problematic. Heavy, aerodynamic satellites such as GOCE were designed specifically to minimise the effect of drag. Satellites with higher power requirements (hence larger solar panels), and lower launch masses (to be cheaper) have commensurately higher area-to-mass ratios, and hence drag modelling errors become more serious. LEO satellites, in particular the many polar orbiters, can take as little as 90 minutes to orbit the Earth. This means they can pass repeatedly through patches of long-lived density instability during a single day, but these are not properly characterised by existing satellite drag atmosphere models.

Drag measurements are also used to deduce thermospheric density as can be seen from Equation 6. Here $\underline{a}$ is satellite acceleration; A_{eff} is effective cross-sectional area along the ram direction; C_{d} is satellite drag coefficient, and satellite mass m. The total velocity V relative to the atmosphere is given by the unit vector $\underline{\hat{v}}$. The ratio of effective area to mass, and the drag coefficient, are acknowledged to be very difficult to quantify, which is well known by the satellite engineers (e.g. Moe et al., 1995), but less known by the atmospheric community. However, systematic differences between thermospheric densities that are measured by satellite drag and compared with GCMs are already acknowledged (Bruinsma et al, 2014).

$$\underline{a} = -\frac{1}{2}\rho\frac{C_d}{m}A_{eff}V^2\underline{\hat{v}} \tag{6}$$

The upper atmosphere is in a state of diffusive equilibrium, where lighter atoms, mainly atomic oxygen, hydrogen and helium dominate. The interaction of gases with surface material may be influenced by the upwelling of molecular gases, mainly molecular nitrogen and molecular oxygen. These may also affect the transfer of momentum to the satellites in a subtle way as indicated by an adaption of the momentum transfer integral from Schunk and Nagy (equation 4.89b, 2009) as shown in equation 2. Here $\delta\underline{M}_i$ is the momentum transferred to particle *i*, with mass m_i and number density n_i moving with velocity $\underline{u}_i$ in time δt by the *n*th particle moving with velocity $\underline{u}_n$. In this case the particle *i* is the satellite, and we should consider the change in momentum transfer due to up/downwelling moving molecular species vertically.

$$\frac{\delta\underline{M}_i}{\delta t} = -\sum_n n_i m_i \upsilon_{in}(\underline{u}_i - \underline{u}_n) \tag{7}$$

The CMAT2 simulation in section 4 demonstrated that the neutral density can be enhanced by up to 20% during the localised heating event. The upwelling will also bring up molecular species (N_2 and O_2) and change the chemical composition of the height region. This is not significant at typical LEO altitudes which are usually > 400 km, but may be of concern for controlled deorbiting of satellites at the end of their life-times.

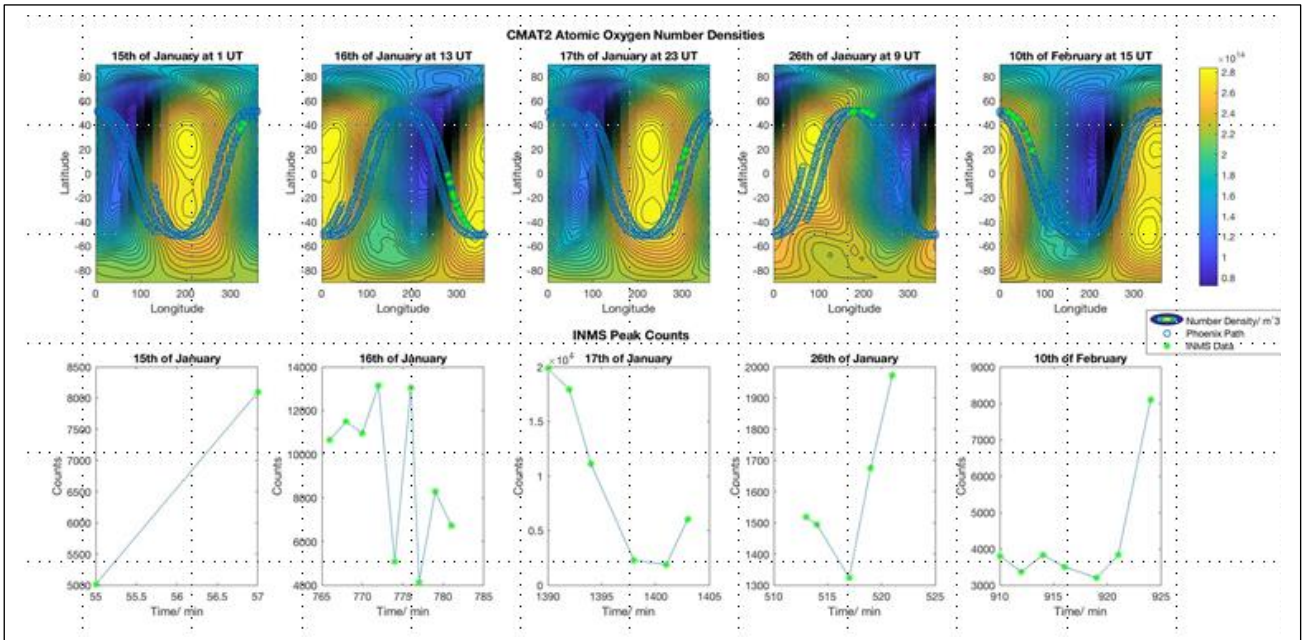

Figure 20 Preliminary results of O+ number densities measured by the INMS on the PHOENIX CubeSat compared with the CMAT2 model of atomic oxygen at constant height 300 km. (Apsit, 2018)

Figure 19 shows the first data from the miniaturised Ion Neutral Mass Spectrometer on the Phoenix CubeSat collected between 15 January and 10 February 2018 (Apsit, 2018). The top row shows latitude-longitude plots of the Phoenix orbital paths in blue circles, on top of CMAT2 simulations of the atomic oxygen density. The green circles show where the data were collected during the orbit. The bottom row shows the raw INMS counts against time. The INMS was monitoring atomic oxygen ions O^+, but we are still in the process of validating and calibrating the data. We successfully won radar time for 4 days of Incoherent Scatter World Days (15-16 January and 12-13 June 2018) and are

working on setting up comparisons with Millstone Hill radar. The QB50 mission was a proof of concept mission and technology demonstrator for launching multiple CubeSats near simultaneously. These are the first in-situ mass spectrometer measurements for over 30 years. The prospect of multiple such relatively cheap instruments on CubeSats (compared with single big satellite missions) has the potential to provide valuable multi-point in-situ measurements to test empirical models and ground-based observations.

4 Conclusions

The LEO region of space has become critically congested with satellites and debris due to increasing numbers of commercial and scientific launches. Controlled re-entry or removal to a far distant parking orbit are the legal requirements nowadays. Our concern was to examine the "lumpiness" of the upper atmosphere, which will have some as yet unquantified influence on satellite drag, and the prediction of orbits during Very Low Earth Orbits, and re-entry. We have demonstrated evidence of large and sustained upwelling and downwelling of the thermosphere at auroral latitudes using measurements of winds by FPIs. Large vertical winds have long been a contentious issue since the common assumption is that the thermosphere is in a state of hydrostatic equilibrium, i.e. near zero vertical motion. We have shown that the FPI observations were corroborated by independent measurements of the ionosphere using Incoherent Scatter Radars, and by an independent wide-field FPI (SCANDI) measuring the horizontal wind field. The energy required to sustain such vertical movement is also feasible. We have also demonstrated that a hydrostatic GCM such as CMAT2 is capable of recreating vertical motions of the same size as observed by the FPI. Previous attempts to achieve upwellings to recreate the CHAMP satellite observations of a doubling of density were achieved using a non-hydrostatic model (GITM). It is currently a major goal of the atmospheric community to extend lower atmosphere models upwards to cover the whole altitude range of the fluid atmosphere. Lower atmosphere models, such as the UK Met Office Unified Model, are non-hydrostatic in order to model the large vertical convection cells typical of the troposphere. It is anticipated that extending non-hydrostatic models upward will allow a better representation of the vertical motions observed by FPIs. In the meantime, we have demonstrated that we can achieve a reasonable outcome with a hydrostatic model from which to investigate and quantify the possible satellite perturbations from a non-smoothly varying atmosphere.

5 Acknowledgements

In addition to the direct contribution to this project by Dr Ian McWhirter (instrumentation) and David Johnson (modelling), the author acknowledges contributions from Dr Amy Ronksley and MSci project students: Anna Apsit and Jennifer Hall. Also Prof Dhiren Kataria for QB50 data. EISCAT is an international association supported by research organisations in China (CRIRP), Finland (SA), Japan (NIPR and STEL), Norway (NFR), Sweden (VR), and the United Kingdom (NERC). We thank the institutes who maintain the IMAGE Magnetometer Array: Tromsø Geophysical Observatory of UiT the Arctic University of Norway (Norway), Finnish Meteorological Institute (Finland), Institute of Geophysics Polish Academy of Sciences (Poland), GFZ German Research Centre for Geosciences (Germany), Geological Survey of Sweden (Sweden), Swedish Institute of Space Physics (Sweden), Sodankylä Geophysical Observatory of the University of Oulu (Finland), and Polar Geophysical Institute (Russia).

6 References

Akmaev, R.A. Whole Atmosphere Modelling: Connecting Terrestrial and Space Weather, Rev.Geophys., 49, RG4004. DOI 10.1029/2011RG000364, 2011

Apsit, A., QB50 – CubeSat observations of the lower thermosphere during a decaying satellite orbit, UCL MSci 4th year undergraduate project, (supervisors **A.L.Aruliah** and D.Kataria), March 2018

Aruliah, A.L., E.M.Griffin, A.D.Aylward, E.A.K.Ford, M.J.Kosch, C.J.Davis, V.S.C.Howells, E.Pryce, H.Middleton, J.Jussila, First direct evidence of meso-scale variability on ion-neutral dynamics using co-located tristatic FPIs and EISCAT radar in Northern Scandinavia, EISCAT workshop special issue Annales Geophys., 23, 147-162, 2005

Aruliah A.L., The role of neutral atmospheric dynamics in cusp density and ionospheric patch formation, Award number FA8655-11-1-3038, 2012

Aruliah A.L., The role of neutral atmospheric dynamics in cusp density and ionospheric patch formation – 2nd campaign, Award number FA8655-13-1-3012, 2013

Aruliah, A.L., The consequences of the geomagnetic field for the thermosphere, invited talk at the Royal Astronomical Society specialist discussion meeting on "Geomagnetic field dynamics and structure on timescales from minutes to decades", 2014

Aruliah, A.L., A. Ronksley, D. Johnson, H.C.Carlson, Multi-Instrument and Modelling Study of Small-Scale Upwelling and Density Changes in the Auroral Thermosphere-Ionosphere Region, European Geophysical Union meeting, 2015

Aruliah A.L., An observational and modelling study of upwelling in the auroral thermosphere, Award number FA9550-15-1-0105, 2016

Bowman, B.R., W.K.Tobiska, F.A.Marcos, C.Valladares, The JB2006 empirical thermospheric density model, JASTP, 70, 774-793, 2008

Bruinsma, S.L., N. Sánchez-Ortiz, E. Olmedo, N. Guijarro (2012), Evaluation of the DTM-2009 thermosphere model for benchmarking purposes, J. Space Weather Space Climate, 2, A04 DOI: 10.1051/swsc/2012005

Burnside R.G., F.A.Herrero, J.W.Meriwether Jnr., J.C.G.Walker, Optical Observations of Thermospheric Dynamics at Arecibo, JGR, 86, 5532-5540, 1981

Carignan, G.R., Block, B.P., Maurer, J.C., Hedin, A.E., Reber, C.A., Spencer, N.W., 1981. The neutral mass spectrometer on Dynamics Explorer. Space Sci. Instrum. 5, 429–441.

Carlson, H. C., T. Spain, A. Aruliah, A. Skjaeveland, and J. Moen, First-principles physics of cusp/polar cap thermospheric disturbances, Geophys. Res. Lett., 39, L19103, doi:10.1029/2012GL053034, 2012a

Carlson, H. C., T. Spain, A. Aruliah, A. Skjaeveland, and J. Moen, Why Thermospheric Density/Drag Should Double Over the Cusp, AGU 2012b

Cosgrove, R. B., et al. (2014), Empirical model of Poynting flux derived from FAST data and a cusp signature, J.Geophys. Res. Space Physics,119, 411–430, doi:10.1002/2013JA019105.

Dee, D. P., S. M. Uppala et al. (2011). The ERA-Interim reanalysis: configuration and performance of the data assimilation system. Quart. J. Roy. Met. Soc. 137(656), 553-597.

Demars, H.G., R.W.Schunk, Thermospheric response to ion heating in the dayside cusp, JASTP, 69, 649-660, 2007

Deng, Y., T. J. Fuller-Rowell, A. J. Ridley, D. Knipp, and R. E. Lopez (2013), Theoretical study: Influence of different energy sources on the cusp neutral density enhancement, *J. Geophys. Res. Space Physics*, *118*, 2340–2349, doi:10.1002/jgra.50197

Dobbin A. L., E. M. Griffin, A. D. Aylward, and G. H. Millward, 3-D GCM modelling of thermospheric nitric oxide during the 2003 Halloween storm, Ann. Geophys., 24, 2403-2412, 2006

Drob, D. P., et al. (2008), An empirical model of the Earth's horizontal wind fields: HWM07, *J.Geophys. Res.*, 113, A12304, doi:10.1029/2008JA013668.

Dryland, Margit, Multi-instrument studies of polar mesopause region temperature and airglow variability, PhD thesis, University Centre in Svalbard, 2010

England, S. L., A review of the effects of non-migrating atmospheric tides on the Earth's low latitude ionosphere. Space Sci. Rev., 168, 211-236, doi:10.1007/s11214-011-9842-4, 2012

Ford, E. A. K.; Aruliah, A. L.; Griffin, E. M.; McWhirter, High time resolution measurements of the thermosphere from Fabry-Perot Interferometer measurements of atomic oxygen, Annales Geophys., 25, 1269 – 1278, 2007

Förster, M. A.A.Namgaladze, R.Y.Yurik, Thermospheric composition changes deduced from geomagnetic storm modelling, GRL, 26, 2625-2628, 1999

Hall, J., Density structures of the thermosphere and how this affects satellite orbits, MSci 4th year project report, 2016

Harris, M. J.; Arnold, N. F.; Aylward, A. D., (2002), A study into the effect of the diurnal tide on the structure of the background mesosphere and thermosphere using the new coupled middle atmosphere and thermosphere (CMAT) general circulation model, *Ann. Geophys., 20*, 225-235.

Hoppel, K. W., N. L. Baker, L. Coy, S. D Eckermann, J. P. McCormack, G. E. Nedoluha, E. Siskind. Assimilation of stratospheric and mesospheric temperatures from MLS and SABER into a global NWP model. Atmos. Chem. Phys., 8, 6103-6116

Johnson, D., Atmospheric coupling using the Newtonian Relaxation technique, PhD to be submitted Dec 2016

Lühr, H.; Rother, M.; Köhler, W.; Ritter, P.; Grunwaldt, L., Thermospheric up-welling in the cusp region: Evidence from CHAMP observations, Geophys. Res. Lett., Vol. 31, No. 6, L06805, 10.1029/2003GL019314, 2004

McKay-Bukowski, D., et al, KAIRA: The Kilpisjarvi Atmospheric Imaging Receiver Array – System overview and first results, IEEE Transactions on Geoscience and remote sensing, 53, 1440-1451, 2015.

Moe, Mildred.M., Steven D. Wallace, Kenneth Moe, The upper mesosphere and lower thermosphere, A review of experiment and theory, Geophysical Monograph 87, 1995

Picone, J.M., Hedin, A.E., Drob, D.P., Aikin, A.C. NRLMSISE-00 empirical model of the atmosphere:Statistical comparisons and scientific issues, J.Geophys.Res. 107, A12, 1468, 2002.

Price, G.D., F.Jacka, The influence of geomagnetic activity on the upper mesosphere/lower thermosphere in the auroral zone. I. Vertical winds, J.Atmos.Terr.Phys., 53, 909-922, 1991

Ridley, A.J., Y.Deng, G.Toth, The global ionosphere-thermosphere model, JASTP, 68, 839-864, 2006

Ronksley, Amy, Optical remote sensing of mesoscale thermospheric dynamics above Svalbard and Kiruna, PhD thesis, UCL, 2016

St.-Maurice J.-P., W.B.Hanson, Ion Frictional Heating at High Latitudes and Its Possible Use for an In Situ Determination of Neutral Thermospheric Winds and Temperatures, JGR, 87, 7580-7602, 1982

Schunk, R. W. (1975), Transport equations for aeronomy, Planet. Space Sci., 23, 437–485.

Schunk, R.W. and A.F.Nagy, Ionospheres: Plasma physics, and chemistry, Cambridge University Press, 2009

Tanskanen, E.I. (2009): A comprehensive high-throughput analysis of substorms observed by IMAGE magnetometer network: Years 1993-2003 examined. J. Geophys. Res., 114, A05204, doi:10.1029/2008JA013682.

Telford, P. J., P. Braesicke, O. Morgenstern, J. A. Pyle (2008). Technical note: Description of the assessment of a nudged version of the new dynamics Unified Model. Atmos. Chem. Phys., 8, 1701-1712

Vallado, D.A., D.Finkleman, A critical assessment of satellite drag and atmospheric density modelling, American Institute of Aeronautrics and astronautics,Acta Astronautica, 95, 141-165, 2014

Vickers, H., M. J. Kosch, E. Sutton, Y. Ogawa, and C. La Hoz (2013), Thermospheric atomic oxygen density estimates using the EISCAT Svalbard Radar, J. Geophys. Res. Space Physics, 118, 1319–1330, doi:10.1002/jgra.50169.

Winser K.J., A.D.Farmer, D.Rees, A.L.Aruliah, Ion-Neutral Dynamics in the High Latitude Ionosphere: First Results from the INDI Experiment, JATP, 50, 369-377, 1988

Related talks and posters prepared/presented during period of grant

Aruliah, A.L., Matthias Förster, Rosie Hood, Amy Ronksley, A puzzling difference when comparing ground-based FPI and CHAMP satellite thermospheric winds in the auroral region, Presentation (talk) during field trip to staff at Sodankylä Geophysical Observatory, Finland

Aruliah, A.L., Matthias Förster, Eelco Doornbos, Rosie Hood and **David Johnson**, Comparing High-Latitude Thermospheric Winds From FPI and CHAMP Accelerometer Measurements, New (poster) Orleans, AGU 2017

Aruliah, A.L., David Johnson, Dhiren Kataria, Theophile Brochant De Villiers, Robert Wicks, and Davide Masutti, Anna Apsit, Jennifer Hall, Liberty Jairaj-Jacklin, Carsten Sharlemann, Thomas Dorn, and Bjørn Lybekk and Ming-Yang Hong, An in-situ multi-point observation of the thermosphere using CubeSats coordinated with ground-based instruments, and model studies, , **(invited talk)** UK MIST meeting at the University of Southampton, March 2018

Aruliah, A.L. (Physics & Astronomy), Monitoring Space Weather, UCL Space Week Workshop: Big Data – A Space Perspective **(invited talk)**, April 2018

Aruliah, A.L., CubeSats as "Space Weather Balloons", Whole Atmosphere Modelling workshop: Developments in the context of Space Weather **(invited talk)** Tres Cantos, Spain, June 2018

Johnson, D., A.L.Aruliah, A.D.Aylward, D.Kataria, W.Wicks, Cross-calibrating thermospheric densities using QB50 flotilla of CubeSat orbits and measurements, 9th European CubeSat Symposium, Nov 2017

McWhirter, I, **A Aruliah**, Forecasting space weather: The need for ground-based observations in addition to satellite measurements, 44th Annual European Meeting on Atmospheric Studies by Optical Methods, (talk) 4-8 September 2017, Barcelona, Spain

4th year MSci projects during period of grant

Jairaj-Jacklin, L., An analysis of in-situ and ground-based derived thermospheric densities over the EISCAT Svalbard Radar, UCL MSci 4th year undergraduate project, (supervisor **A.L.Aruliah**), March 2017

Apsit, A., QB50 – CubeSat observations of the lower thermosphere during a decaying satellite orbit, UCL MSci 4th year undergraduate project, (supervisors **A.L.Aruliah** and D.Kataria), March 2018

7 List of Symbols, Abbreviations and Acronyms

$\underline{B}$	Earth's magnetic field vector
Bx	x-component of the Earth's magnetic field
CMAT2	Coupled Middle Atmosphere Thermosphere model
EISCAT	European Incoherent Scatter Radar
ESR	EISCAT Svalbard Radar
FIPEX	Flux-Ø-Probe Experiment
FPI	Fabry Perot Interferometer
GITM	Global Ionosphere-Thermosphere Model
IMAGE	International Monitor for Auroral Geomagnetic Effects
INMS	Ion Neutral Mass Spectrometer
ISR	Incoherent Scatter Radar
KAIRA	Kilpisjärvi Atmospheric Imaging Receiver Array
KEOPS	Kiruna ESRANGE Optical Platform Site, Sweden
KHO	Kjell Henriksen Observatory, Svalbard
MSP	Meridional Scanning Photometer
MNLP	Multi-Needle Langmuir Probe
Ne	Electron densities
SCANDI	Scanning Doppler Imager
SGO	Sodankylä Geophysical Observatory, Finland
Te	Electron temperatures
Ti	Ion temperatures
Tn	Thermospheric neutral temperatures
UCL	University College London, UK
Un	Thermospheric neutral wind velocity
Vi	Ionospheric plasma velocity
$V_{//}$	Ionospheric plasma speeds parallel to the magnetic field line